

# Journal of Geophysical Research: Solid Earth

## RESEARCH ARTICLE

10.1002/2015JB012588

**Key Points:**

- Catalog of 106 moment tensors using body waves and surface waves
- Moment tensor uncertainty estimates provided for 21 earthquakes
- Choices in the waveform misfit function influence the moment tensor solution

**Supporting Information:**

- Supporting Information S1
- Supporting Information S2
- Supporting Information S3
- Supporting Information S4
- Supporting Information S5

**Correspondence to:**V. Silwal,  
vsilwal@alaska.edu**Citation:**Silwal, V., and C. Tape (2016), Seismic moment tensors and estimated uncertainties in southern Alaska, *J. Geophys. Res. Solid Earth*, 121, 2772–2797, doi:10.1002/2015JB012588.

Received 8 OCT 2015

Accepted 16 MAR 2016

Accepted article online 24 MAR 2016

Published online 27 APR 2016

## Seismic moment tensors and estimated uncertainties in southern Alaska

**Vipul Silwal<sup>1</sup> and Carl Tape<sup>1</sup>**<sup>1</sup>Geophysical Institute and Department of Geosciences, University of Alaska, Fairbanks, Alaska, USA

**Abstract** We present a moment tensor catalog of 106 earthquakes in southern Alaska, and we perform a conceptually based uncertainty analysis for 21 of them. For each earthquake, we use both body waves and surface waves to do a grid search over double couple moment tensors and source depths in order to find the minimum of the misfit function. Our uncertainty parameter or, rather, our confidence parameter is the average value of the curve  $\mathcal{P}(V)$ , where  $\mathcal{P}(V)$  is the posterior probability as a function of the fractional volume  $V$  of moment tensor space surrounding the minimum misfit moment tensor. As a supplemental means for characterizing and visualizing uncertainties, we generate moment tensor samples of the posterior probability. We perform a series of inversion tests to quantify the impact of certain decisions made within moment tensor inversions and to make comparisons with existing catalogs. For example, using an L1 norm in the misfit function provides more reliable solutions than an L2 norm, especially in cases when all available waveforms are used. Using body waves in addition to surface waves, as well as using more stations, leads to the most accurate moment tensor solutions.

### 1. Introduction

The seismic moment tensor, visualized as a beach ball, represents the radiation pattern for a point-source earthquake and plays an important role within the field of seismology [e.g., Isacks *et al.*, 1968]. Moment tensors are used to interpret the style of faulting and deformation in active tectonic settings, they are used within seismic wavefield simulations to estimate ground motions in a particular region, and they are used within earthquake-based tomographic inversions that seek to improve seismic velocity models. Despite these fundamental purposes, there have been few insights into how to characterize the uncertainty of moment tensors [Riedesel and Jordan, 1989; Valentine and Trampert, 2012; Käufel *et al.*, 2014; Stähler and Sigloch, 2014]. In this paper we apply a new approach for estimating uncertainties [Tape and Tape, 2016] to a set of 21 earthquakes in southern Alaska (Figures 1 and 2). We also present moment tensor solutions for an additional 85 smaller earthquakes to form a catalog of 106 events.

We could have chosen any set of recorded earthquakes for our uncertainty analysis, but southern Alaska provides several advantages. First, it is a region of active tectonics and high seismicity rates (Figure S1 in the supporting information) with events occurring throughout the crust and within the slab down to depths of 200 km. Second, there is a good network of broadband seismic stations, especially during the time period of interest. Third, there are two existing moment tensor catalogs using two different techniques (section 2.1); this allows us to compare different inversion algorithms and to compare the various choices made within these algorithms. Finally, we are interested in better understanding the tectonics of this region, and we are interested in using our moment tensors within a tomographic inversion using earthquakes, wavefield simulations, and adjoint methods [e.g., Tape *et al.*, 2009]. One of the most prominent tectonic features within our region of interest (Figure 1) is the Cook Inlet fore-arc basin, one of the largest in the world. The basin poses challenges when performing waveform fits between data and synthetics at the stations in and around the basin.

In our study we assume that each earthquake is a shear dislocation that can be modeled as a double couple moment tensor. A double couple moment tensor is a  $3 \times 3$  symmetric matrix whose eigenvalues are  $(\lambda, 0, -\lambda)$ . We are concerned with estimating the magnitude and orientation (strike, dip, and rake) of the moment tensor. Alternative terms for double couple moment tensors are “fault-plane solution” or “focal mechanism.” Our approach to moment tensor estimation can also be applied to “full” moment tensors, which contain an additional two parameters. The full moment tensor representation allows for modeling oblique opening across faults [e.g., Aki and Richards, 1980; Dufumier and Rivera, 1997; Tape and Tape, 2013].

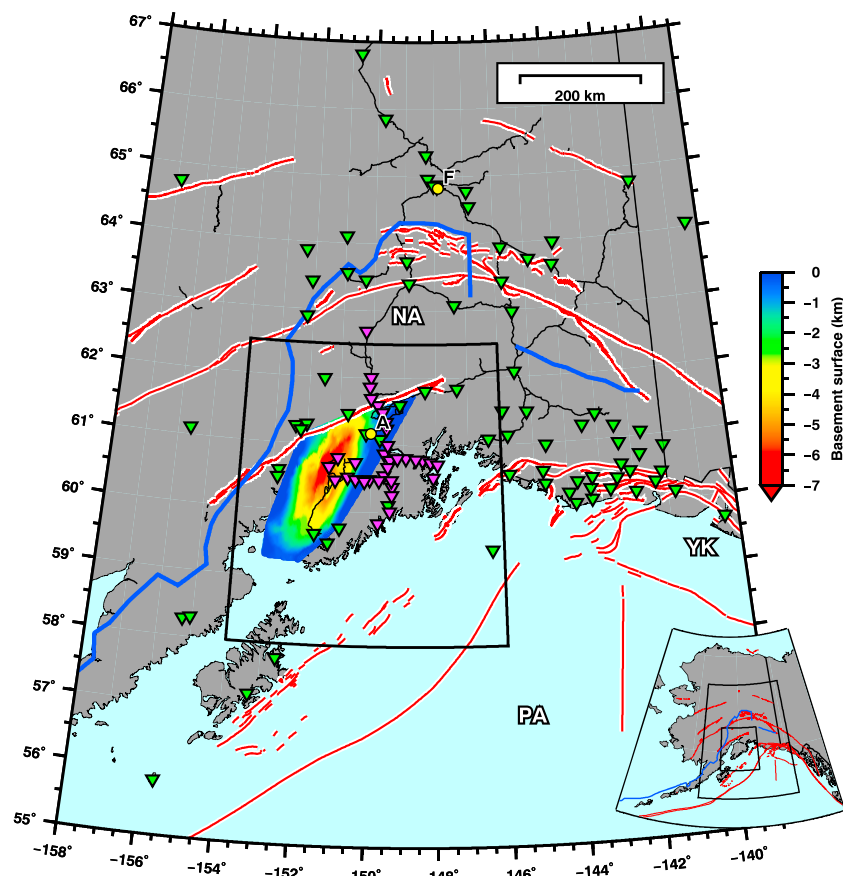


**Figure 1.** Broadband station coverage for the time period of this study, 15 August 2007 to 15 August 2009. The permanent stations in the regional network are plotted green; the MOOS stations are plotted magenta. Stations within 500 km of each epicenter were used for computing the moment tensor solution. The Tertiary basement surface of Cook Inlet basin is color coded for depth [Shellenbaum *et al.*, 2010]. Labels: A = Anchorage, F = Fairbanks, PA = Pacific plate, NA = North American plate, and YK = Yakutat block. See Figure S1 for the seismicity distribution in the region. See Figure 2 for the moment tensor beach balls inside the study region (inner box).

Seismic moment tensors are routinely estimated using different approaches, which can be divided into two broad categories on the basis of data used:

1. High-frequency body waves measurements, such as the polarity of (first-motion)  $P$  waves or the amplitude ratios of  $S$  to  $P$  waves. These observations can be extracted readily from catalogs containing  $P$  and  $S$  arrival times. Two examples of codes that estimate double couple moment tensors from these data are HASH [Hardebeck and Shearer, 2002] and FPFIT [Reasenberg and Oppenheimer, 1985].
2. Filtered seismic waveforms. Other moment tensor inversions involve comparing filtered synthetic waveforms with filtered recorded waveforms. Typically, some portion of the full waveform is used (e.g.,  $P$  wave or surface wave). Examples of this approach are Global Centroid Moment Tensor (GCMT) [Ekström *et al.*, 2012], Time Domain Moment Tensor (TDMT) [Dreger *et al.*, 1998; Dreger and Woods, 2002], cut-and-paste (CAP) [Zhu and Helmberger, 1996], and W-phase [Duputel *et al.*, 2012].

The method of Dreger *et al.* [1998] is the most widely used algorithm for regional moment tensor determination. This method (Time Domain Moment Tensor INVersion Code, TDMT\_INV), which uses relatively long-period surface waves (10–50 s) has been implemented in Alaska [Ratchkovski and Hansen, 2002], western Canada [Ristau *et al.*, 2007], Southern California [Clinton *et al.*, 2006], Japan [Fukuyama *et al.*, 1998; Fukuyama and Dreger, 2000], New Zealand [Ristau, 2008], Spain [Rueda and Mezcua, 2005], and Italy [Scognamiglio *et al.*, 2009], and probably elsewhere. The algorithm constrains moment tensors to be deviatoric. The Alaska Earthquake Center (AEC) uses TDMT to produce their moment tensor catalog, including 21 analyzed in our study. We use the notation  $M_{\text{AEC}}$  to denote a moment tensor in the AEC moment tensor catalog derived using TDMT.

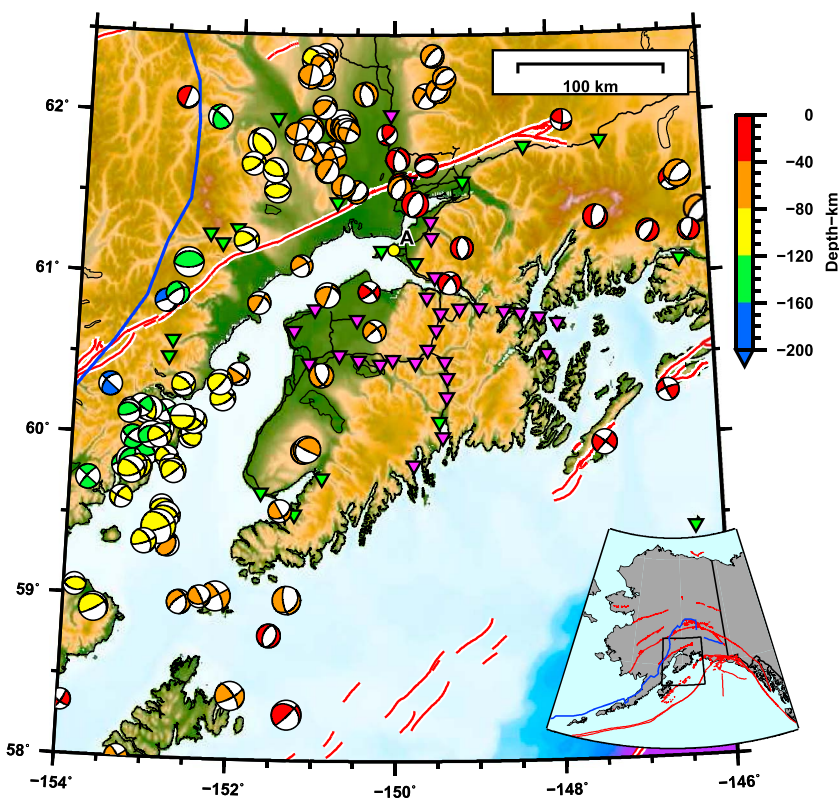


**Figure 2.** Seismotectonic setting of south central Alaska showing the 106 moment tensor solutions obtained in this study. Our catalog contains all earthquakes in this region from 15 August 2007 to 15 August 2009 with  $M_w \geq 3.5$  and for which an AEC first-motion solution was available. Inverted green triangles are the permanent stations in Alaska during this time period, and magenta are the temporary stations deployed during the MOOS array [Christensen et al., 2008; Li et al., 2013]. The heavy blue line marks the lateral extent of slab seismicity, and the red lines delineate the active faults [Koehler et al., 2012].

An example of an algorithm that uses first-motion polarities to determine double couple moment tensors is FPFIT [Reasenberg and Oppenheimer, 1985]. This algorithm uses weighted sum of first-motion polarity differences (between observed and predicted) to find the global minimum and local minima. The uncertainty in each solution parameter is estimated using the 90% confidence interval for the normalized misfit function (0 to 1). The AEC routinely uses FPFIT to estimate double couple moment tensors for earthquakes, including 85 analyzed in our study. We use the notation  $M_{fm}$  to denote a moment tensor from the AEC first-motion catalog derived using FPFIT.

The “cut-and-paste” (CAP) method of Zhu and Helmberger [1996] uses both surface waves and body waves from seismic waveforms filtered over relatively short periods, for example, 3–10 s of Tan et al. [2006] or 5–100 s of Zhu and Helmberger [1996]. The body wave measurements are for the “PnI” waveform which includes multiple paths that follow the arrival of the direct P [Helmberger and Engen, 1980]; this is measured on the vertical and radial components. The surface wave measurements target the Rayleigh wave (vertical and radial components) and the Love wave (transverse component). Based on catalog comparisons in Tape et al. [2009, Appendix D], as well as our desire to fit as much of the seismic wavefield as possible, we chose to use CAP within this study. Details on CAP are presented in sections 2.2–2.4.

Most of the inversion methods discussed above do not have a clear approach for estimating uncertainties in moment tensors. The most common method for estimating uncertainties involves “bootstrapping,” which involves resampling the data and reinverting the moment tensor repeatedly to obtain a set of possible solutions [e.g., Nayak and Dreger, 2014; Ross et al., 2015].

Part of the challenge in estimating uncertainties is that the properties of the moment tensor space under consideration are not obvious. The notion of uniformly distributed moment tensors and the closely related notion of volumes in moment tensor space need to be clarified. For us the space of moment tensors under

consideration is the set of all double couples. For this set *Tape and Tape* [2015] show that uniform orientations give uniformly distributed moment tensors.

We calculate a new uncertainty curve, or rather “confidence curve,”  $\mathcal{P}(V)$ , for each of 21 earthquakes. The function  $\mathcal{P}(V)$ , to be defined precisely in section 3.1, describes how the posterior probability is concentrated around a selected reference tensor within moment tensor space. For example,  $\mathcal{P}(0.1) = 0.9$  means that 90% of the probability is contained within the 10% volume fraction around the reference moment tensor. The curve  $\mathcal{P}(V)$  is calculated from the posterior probability and the fractional volume in moment tensor space. The probability density  $p$  is scaled from a waveform difference misfit function  $\Phi$  as  $p(M) \propto \exp(-\Phi(M))$ . Associated with the curve  $\mathcal{P}(V)$  are two useful scalar quantities: (1) The slope of the curve at the origin is proportional to the probability density at the reference moment tensor. (2) The area  $\mathcal{P}_{AV}$  under the curve, which is the average value of  $\mathcal{P}(V)$ , gives a single measure of confidence.

Our study produces a moment tensor catalog of 106 events in southern Alaska. The catalog is divided into two parts, as explained in section 2.1: Part I (Table 4) and Part II (Table S5). In section 2 we describe our moment tensor inversion, including the estimation of uncertainties. Section 4.1 presents our uncertainty analysis for a single earthquake. Section 5 summarizes a set of comparative inversions for the 21 events. It is intended to provide insights into some of the choices made within moment tensor inversions.

We suggest two alternatives to reading the paper from start to finish. If you are primarily interested in our approach to estimating moment tensor uncertainties, then please focus on sections 3, 4.1, and 7. If you are primarily interested in our assessment of the impact of various decisions made within moment tensor inversions—e.g., type of norm, body waves or surface waves, and number of stations—then please see sections 2.4 and 5.

## 2. Methods

Our objective is to obtain the highest-quality catalog of moment tensors in southern Alaska, primarily for future purposes of earthquake-based seismic tomographic inversion. Our study is centered on data acquired by the MOOS (multidisciplinary observations of subduction) array in the Kenai Peninsula region of south central Alaska [Christensen *et al.*, 2008]. This array had up to 34 broadband stations active between 15 August 2007 and 15 August 2009 and provides the best coverage for studying earthquakes in this region. We also include all permanent broadband stations that were active during this time period; a map of stations is shown in Figure 1. All earthquakes in this study occurred within the bounding box of latitude ( $58^{\circ}, 62.5^{\circ}$ ) and longitude ( $-154^{\circ}, -146^{\circ}$ ) (Figure 2).

### 2.1. Selection of Events and Processing of Waveforms

In addition to estimating the best possible moment tensors in southern Alaska, we are interested in performing comparative studies with existing catalogs. The Alaska Earthquake Center (AEC) maintains two moment tensor catalogs:

1. AEC moment tensor catalog: This catalog contains deviatoric moment tensors for  $M_w \geq 4$  earthquakes. The moment tensors, which we denote by  $M_{AEC}$ , are estimated using the TDMT code [Pasmanos *et al.*, 1996; Dreger *et al.*, 1998].
2. AEC first-motion catalog: This catalog contains double couple moment tensors for  $M_w \geq 3.0$  earthquakes. The moment tensors, which we denote by  $M_{fm}$ , are estimated using the FPFIT code [Reisenberg and Oppenheimer, 1985].

We use these two catalogs as a basis for selecting events in this study. The two catalogs form two parts of our composite catalog of 106 earthquakes:

1. Part I catalog: all 21 events from the AEC moment tensor catalog within our region (Figure 2) and time period of interest. We perform our uncertainty analysis on these events. By focusing on the events in the AEC moment tensor catalog, we can perform direct comparisons between two moment tensor inversion methods: CAP (used here) and TDMT (used by AEC).
2. Part II catalog: 85 events from the AEC first-motion catalog with magnitude  $M_w \geq 3.5$  and within our region and time period of interest. For several of the smaller Part II catalog events we use first-motion polarity observations in order to help constrain the solution. We do not calculate confidence curves for the 85 events, mainly because our current formulation of the misfit function—and subsequent confidence

curve—does not consider first-motion polarities. Our primary goal for the Part I events is to obtain the most reliable moment tensor solutions and to compare them with the solutions obtained by AEC using  $P$  wave polarities only.

We acquired three-component broadband seismic waveforms from the Alaska Earthquake Center and from the MOOS waveform database [Christensen *et al.*, 2008]. For each event we extracted 300 s of waveforms from stations within 500 km of epicentral distance (Figure 1). Waveform processing, including instrument deconvolution between periods 0.04–100 s (using a two-pole Butterworth band-pass filter), was performed using the GISMO Waveform Toolbox for MATLAB [Reyes and West, 2011]. Additional band-pass filtering was applied within the moment tensor grid search algorithm.

## 2.2. Cut-and-Paste (CAP) Approach

The cut-and-paste moment tensor inversion approach of *Zhao and Helmberger* [1994] and *Zhu and Helmberger* [1996] is named for its cutting of sections of synthetic seismograms and pasting them on corresponding portions of observed seismograms. A key feature is that each section of synthetic seismogram is allowed to be time shifted to best match the observed seismogram. By using different time shifts, CAP accounts for some of the errors associated with the seismic velocity model that is assumed. For example, for a given station we might expect a different time shift between data and synthetics for the  $P$  wave, Rayleigh wave, and Love wave. Allowing for different time shifts is especially important when considering a second feature of CAP: different band-pass filters are generally applied to body waves and surface waves.

The seismic waveforms are rotated radial, transverse, and vertical components and are divided into five time windows of body and surface waves: (1) PV: vertical component of the  $P$  wave, (2) PR: radial component of the  $P$  wave, (3) SurfV: vertical component of the Rayleigh wave, (4) SurfR: radial component of the Rayleigh wave, and (5) SurfT: transverse component of the Love wave.

Any of these time windows can be excluded based on the waveform selection criteria (section S2.1).

In our inversions we use three time shifts: one for PV and PR, one for SurfV and SurfR, and one for SurfT. For the 21 Part I events in our catalog (Table 4), we filtered body waves between 1.5 and 4.0 s and allowed a maximum time shift of  $\pm 2$  s, and we filtered surface waves between 16 and 40 s and allowed a maximum time shift of  $\pm 10$  s. For the 85 smaller Part II events in the catalog, we made adjustments to the band-pass filters and time shifts. Our goal was to fit as much of the wavefield as possible, both in terms of the broadest band pass and the greatest sections of time.

## 2.3. Grid Search Moment Tensor Inversion

In a grid search moment tension inversion, one looks for the minimum of a misfit function  $\Phi$  between observed and synthetic seismograms. The CAP approach is distinguished by the details of how  $\Phi$  is assembled from pieces of filtered seismic waveforms. Our synthetic seismograms are computed using a frequency-wave number method based on the Thomson-Haskell Propagator matrix method [*Haskell*, 1964; *Zhu and Rivera*, 2002]. We use the same layered seismic velocity model that is used by the Alaska Earthquake Center for moment tensor inversions and for locating earthquakes (Table S1). Once a misfit function is established, the approach to finding the minimum of the misfit function is a straightforward grid search over the space of model parameters.

We consider five model parameters: earthquake depth  $z$ , earthquake magnitude  $m$ , and moment tensor orientation: strike  $\kappa$ , rake  $\sigma$ , and dip  $\theta$ . We assume that the earthquakes occur as shear faulting without opening; hence, our moment tensors are double couples. We fix the epicenter and origin time as those from the AEC catalog.

The search ranges for our parameters are depth  $z$ :  $z_{\text{AEC}} - 35 \leq z \leq z_{\text{AEC}} + 35$ , where  $z_{\text{AEC}}$  is the depth in the AEC moment tensor catalog; magnitude  $m$ : search within  $\pm 1$  unit of the AEC moment tensor catalog magnitude; strike  $\kappa$ :  $0^\circ \leq \kappa < 360^\circ$ ; rake  $\sigma$ :  $-90^\circ \leq \sigma \leq 90^\circ$ ; and  $h = \cos \theta$ :  $0 < h \leq 1$ , corresponding to dip  $\theta$  ranging from  $0^\circ$  to  $90^\circ$ .

The use of  $h$  instead of dip angle  $\theta$  allows us to obtain uniformly distributed orientations by choosing  $\kappa$ ,  $\sigma$ , and  $h$  uniformly [*Kagan*, 1991; *Tape and Tape*, 2012]. Uniformly distributed orientations give uniformly distributed double couple moment tensors [*Tape and Tape*, 2015].

While our grid search involves five parameters, most of the postprocessing uncertainty analysis involves only the three parameters ( $\kappa$ ,  $\sigma$ , and  $h$ ) that describe the moment tensor orientation. For each earthquake our

### A. Evaluate misfit function between observed and synthetic seismograms

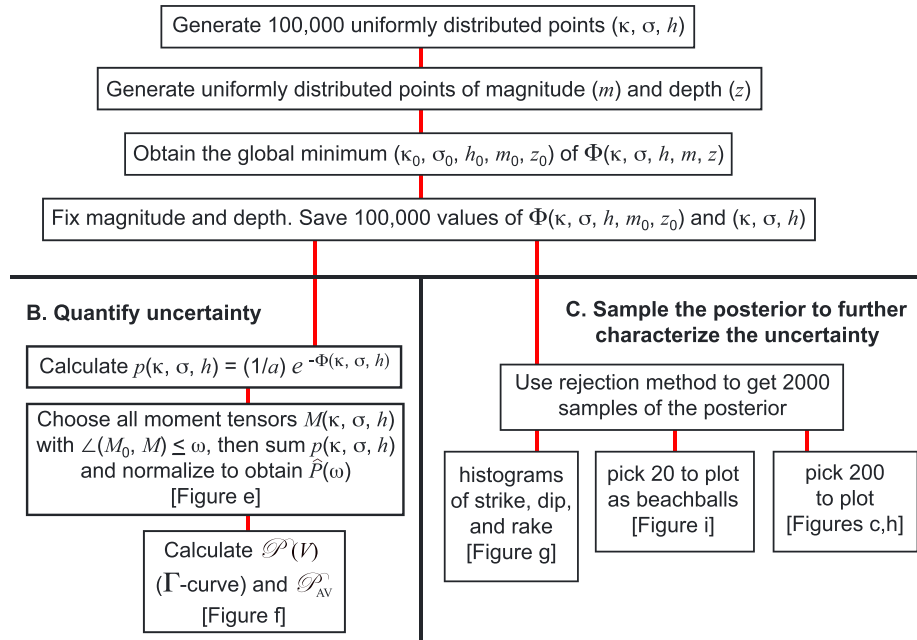


**Figure 3.** Workflow for our uncertainty analysis, such as in Figure 7. The model parameters for the moment tensor inversion are the strike angle  $\kappa$ , the rake (or slip) angle  $\sigma$ , cosine of the dip angle ( $h = \cos \theta$ ), the magnitude ( $m$ ), and depth  $z$ , all with ranges as specified in section 2.3. The uncertainty analysis (parts B and C) begins when we have determined the magnitude and depth of the moment tensor  $M_0$  at the global minimum of the misfit function.

unknown model vector is

$$\mathbf{m} = (\kappa, \sigma, h, m, z)^T. \quad (1)$$

Our goal is to search over this parameter space to obtain the model vector  $\mathbf{m}_0 = (\kappa_0, \sigma_0, h_0, m_0, z_0)$  that minimizes the misfit  $\Phi$ . We let  $M_0$  be the corresponding moment tensor:

$$M_0 = M(\kappa_0, \sigma_0, h_0, m_0, z_0) \quad (2)$$

(The moment tensor  $M_0$  is not to be confused with the scalar seismic moment, also usually denoted by  $M_0$ .)

We can find  $M_0$  either by using a regular grid of points or by using random points. The values of  $M_0$  in our catalog (e.g., Table 4) are based on the regular grid search; the intervals are listed in Table S2. Alternatively, we could have found  $M_0$  from the set of random points used in our uncertainty analysis. The workflow in Figure 3 starts by generating 100,000 random points in the space of  $\kappa$ - $\sigma$ - $h$ . We then choose a regular grid for searching over depth and magnitude (Table S2). We evaluate the misfit function  $\Phi$  at the moment tensors to obtain the minimum.

Our analysis of uncertainties begins at this stage, with both the magnitude  $m = m_0$  and the depth  $z = z_0$  fixed; the analysis therefore only involves the moment tensor orientation, which is determined by  $(\kappa, \sigma,$  and  $h)$ .

#### 2.4. Misfit Function $\Phi$

Let  $s(M)$  represent a predicted time series for a moment tensor  $M$ . We can think of  $s(M)$  as a forward model that will input a moment tensor and output a time series of ground motion on the surface. The underlying physics is wave propagation in a simple layered medium.

Our misfit function measures the difference between recorded seismograms ("data") and modeled seismograms ("synthetics"). Each station records ground motions in three components, which are recorded on three seismograms. Let  $\mathbf{u}$  represent a discretized time series of one component of the seismometer-recorded ground velocity, so  $u_k$  would be the ground velocity at time  $t_k$ . The goal is to find the  $M$  that minimizes the difference between  $\mathbf{u}$  and  $s(M)$ .

Seismograms at each station are split into different time windows. We use  $i$  for the time window index and  $j$  for the station index. We adopt the commonly used L2 norm as a measure of misfit between data and synthetic waveforms. The L2 norm waveform difference within a single time window is given by

$$\phi_{ij}(M) = \left[ (\mathbf{u}_{ij} - s_{ij}(M))^T \mathbf{W}_{ij} (\mathbf{u}_{ij} - s_{ij}(M)) \right]^{1/2}, \quad (3)$$

where the matrix  $\mathbf{W}_{ij}$  is a weighting matrix that can be thought of as an inverse data covariance matrix [e.g., Aster *et al.*, 2012]. For our purposes it is a diagonal square matrix with the same weight factor  $w_{ij}$  on the diagonal. This gives the flexibility of adjusting the weights for any time window.

We define a misfit function for each earthquake. Each earthquake is recorded by  $N_s$  stations. Each seismogram at each station is split into five time windows (PV, PR, SurfV, SurfR, and SurfT). We consider two norms for the misfit function, which we refer to as L1 and L2:

$$\Phi_{L1}(M) = \sum_{j=1}^{N_s} \sum_{i=1}^5 \phi_{ij}(M) \quad (4)$$

$$\Phi_{L2}(M) = \sum_{j=1}^{N_s} \sum_{i=1}^5 \phi_{ij}^2(M). \quad (5)$$

Equation (5) is actually the square of an L2 norm and is what was implemented in the CAP code of Zhu and Helmberger [1996]. We are not directly comparing values of these two norms, rather we are comparing the moment tensors that give the minima. The L1 norm is less sensitive to outliers than the L2 norm [Aster *et al.*, 2012]. The moment tensor that minimizes  $\Phi_{L1}(M)$  may be very different from the one that minimizes  $\Phi_{L2}(M)$ , as we will see later in section 5.1.

In the explanation and notation above we have omitted some details. Each waveform within a synthetic seismogram is time shifted to match the data. Furthermore, the data and synthetics are filtered (identically) over a specified band pass. Finally, there is a built-in weighting of waveforms by source-station distance that allows the more distant stations to have influence comparable to closer stations [Zhu and Helmberger, 1996].

## 2.5. Scaling the Misfit Function

We define a scaled version  $\Phi$  of the L1 norm misfit function by

$$\Phi(M) = \frac{k}{u_{L1}} \Phi_{L1}(M) = \frac{k}{u_{L1}} \sum_{j=1}^{N_s} \sum_{i=1}^5 \phi_{ij}(M), \quad (6)$$

where  $u_{L1}$  is defined in terms of the observed waveforms by

$$u_{L1} = \sum_{j=1}^{N_s} \sum_{i=1}^5 \left[ \mathbf{u}_{ij}^T \mathbf{W}_{ij} \mathbf{u}_{ij} \right]^{1/2}. \quad (7)$$

The reason we need a scale factor in the misfit function is that as with most seismological studies, the errors in the data are poorly known. If we had a good estimate for errors in the data, then our weighting matrix for each time window,  $\mathbf{W}_{ij}$ , could be represented by the inverse data covariance matrix. Furthermore, if we knew how the uncertainties varied with each source-station path, then we could incorporate this information explicitly within the summations in equations (4) and (5). Because these quantities are unknown, we account for the lack of information with the scale factor  $k/u_{L1}$ .

The constant  $k$  is the same for all events. The scaling by  $k/u_{L1}$  does not impact our best fitting moment tensors  $M_0$ , but it does impact our uncertainty analysis; we return to this topic in section 7.2.

### 3. Estimation of Uncertainties

Our uncertainty analysis is summarized in Figure 3 and described below. The notion of distance in the space of moment tensors is important. The (angular) distance between two moment tensors  $X = (x_{ij})$  and  $Y = (y_{ij})$  is defined in terms of their Euclidean inner product:

$$\angle(X, Y) = \cos^{-1} \frac{X \cdot Y}{\|X\| \|Y\|}, \quad (8)$$

where  $X \cdot Y = \sum_{i,j=1}^3 x_{ij} y_{ij}$  and  $\|X\| = \sqrt{X \cdot X}$ .

The moment tensor for the global minimum of the misfit function is denoted by  $M_0$ . We define  $\omega(M)$  to be the distance from  $M_0$  to  $M$ :

$$\omega(M) = \angle(M_0, M). \quad (9)$$

The angle  $\omega(M)$  ranges from  $\omega(M_0) = 0^\circ$  to  $\omega(-M_0) = 180^\circ$ .

Our moment tensor space is taken to be the set of all double couple moment tensors with fixed norm (i.e., fixed magnitude). We denote it by  $\mathbb{M}$ . The probability density  $p$  on  $\mathbb{M}$  is defined from the misfit function by [Tarantola, 2005]

$$p(M) = \frac{1}{a} e^{-\Phi(M)}, \quad a = \int_{\mathbb{M}} e^{-\Phi(M)} dM, \quad (10)$$

where, for us,  $\Phi(M) = \Phi(\mathbf{m}(\kappa, \sigma, h, m_0, z_0))$  and  $M = M(\kappa, \sigma, h)$ . The probability that the true moment tensor for the earthquake is in a given subset  $\mathbb{A}$  of  $\mathbb{M}$  is the integral of  $p$  over  $\mathbb{A}$ :

$$P(\mathbb{A}) = \frac{\int_{\mathbb{A}} e^{-\Phi(M)} dM}{\int_{\mathbb{M}} e^{-\Phi(M)} dM}. \quad (11)$$

We sometimes refer to the probability  $P$  as the posterior probability. The “prior” probability would then be the homogeneous probability, that is, the fractional volume.

#### 3.1. Quantification of Uncertainty

Our confidence curve  $\mathcal{P}(V)$  is from Tape and Tape [2016]. The curve depends on a reference moment tensor, which will usually be the moment tensor  $M_0$  with lowest misfit (or highest probability density). To define  $\mathcal{P}(V)$ , we first let  $\mathbb{N}(\omega)$  be the neighborhood of  $M_0$  consisting of moment tensors within angular radius  $\omega$  of it. We then let  $\hat{P}(\omega)$  and  $\hat{V}(\omega)$  be the probability and fractional volume of  $\mathbb{N}(\omega)$ . Then  $\mathcal{P}(V)$  is defined to be the probability that the true moment tensor for the earthquake lies in the neighborhood of  $M_0$  that has volume  $V$ . That is, as illustrated in Figure 4,

$$\mathcal{P}(V) = \hat{P}(\omega) \text{ when } \hat{V}(\omega) = V. \quad (12)$$

The confidence curve  $\mathcal{P}(V)$  shows to what extent the probability in moment tensor space is concentrated around the tensor  $M_0$ . For a high-quality event, we would expect  $\mathcal{P}(V)$  to be near unity for some small  $V$ ; equivalently, the curve  $\mathcal{P}(V)$  should resemble the Greek letter  $\Gamma$ .

The average value of  $\mathcal{P}(V)$  is

$$\mathcal{P}_{AV} = \int_0^1 \mathcal{P}(V) dV. \quad (13)$$

The closer  $\mathcal{P}_{AV}$  is to unity, the better.

To calculate  $\mathcal{P}(V)$  from equation (12), we need both  $\hat{V}(\omega)$  and  $\hat{P}(\omega)$ . To get  $\hat{V}(\omega)$  (approximately), we can construct a sequence  $M_1, M_2, \dots, M_N$  of uniformly distributed moment tensors in  $\mathbb{M}$ ; according to Tape and Tape [2015], this can be done by choosing each of the corresponding  $\kappa_i, \sigma_i$ , and  $h_i$  uniformly. Uniformity of the

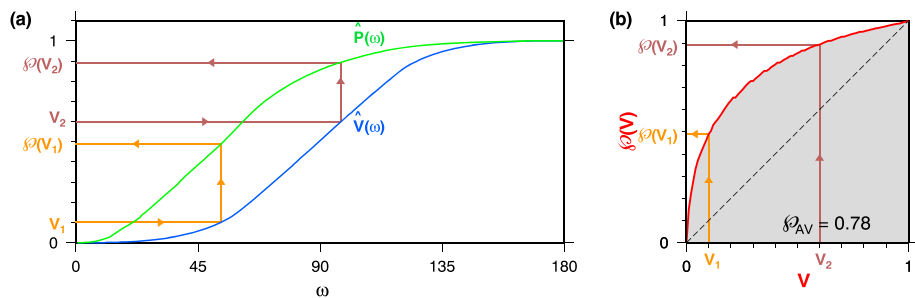


**Figure 4.** Construction of the confidence curve  $\mathcal{P}(V)$  for a moment tensor  $M_0$ . (a) The fractional volume and probability curves  $\hat{V}(\omega)$  and  $\hat{P}(\omega)$ . The value  $\mathcal{P}(V)$  is defined in terms of  $\hat{V}(\omega)$  and  $\hat{P}(\omega)$  by requiring that  $\mathcal{P}(V) = \hat{P}(\omega)$  when  $\hat{V}(\omega) = V$ , as indicated by the arrows. The number  $\hat{V}(\omega)$  is the fractional volume of the neighborhood  $\mathbb{N}_{M_0}(\omega)$  of moment tensors within angular distance  $\omega$  of  $M_0$ , and  $\hat{P}(\omega)$  is likewise the probability of  $\mathbb{N}_{M_0}(\omega)$ . Hence,  $\mathcal{P}(V)$  is the probability that the true moment tensor for the earthquake lies in the neighborhood of  $M_0$  that has volume  $V$ ; large  $\mathcal{P}(V)$  for small  $V$  is desirable. (b) The confidence curve  $\mathcal{P}(V)$ . The orange and brown trajectories correspond to those in Figure 4a. The area under the curve is our confidence parameter  $\mathcal{P}_{\text{Av}}$ . The 45° line (dashed) would be  $\mathcal{P}(V)$  if the probability had been homogeneous.

moment tensors  $M_i$  in  $\mathbb{M}$  means that subsets of  $\mathbb{M}$  having equal volumes should contain equal numbers of the  $M_i$ . Since  $\hat{V}(\omega)$  is the fractional volume of  $\mathbb{N}(\omega)$ , then

$$\hat{V}(\omega) \approx \frac{n(\omega)}{N}, \quad (14)$$

where  $n(\omega)$  is the number of the  $M_i$  with  $\angle(M_0, M_i) \leq \omega$ . Thus, the fractional volume  $\hat{V}(\omega)$  is found by counting the number of moment tensors  $M_i$  within the expanding neighborhood defined by  $\omega$ .

Finding  $\hat{P}(\omega)$  is only slightly more involved. Since  $\hat{P}(\omega)$  is the probability of the set  $\mathbb{N}(\omega)$ , it is given by equation (11) with  $\mathbb{N}(\omega)$  in place of  $\mathbb{A}$ . Using  $M_1, M_2, \dots, M_N$  as before, we can replace the ratio of the integrals in equation (11) with a ratio of sums:

$$\hat{P}(\omega) \approx \sum_{\angle(M_0, M_i) \leq \omega} e^{-\Phi(M_i)} / \sum_{i=1}^N e^{-\Phi(M_i)}. \quad (15)$$

Notice that if the probability  $P$  were the homogeneous probability, for which the function  $p$  would be constant, then equation (15) would reduce to equation (14), and  $\hat{P}(\omega)$  would coincide with  $\hat{V}(\omega)$ .

The fractional volume  $\hat{V}(\omega)$  depends neither on  $M_0$  nor on the earthquake. Its derivative  $\hat{V}'(\omega)$  has a mesa-like shape. Values of  $\hat{V}'(\omega)$  are tabulated in Appendix A of *Tape and Tape* [2016].

### 3.2. Samples of the Posterior Probability

There is an alternate perspective on the calculation of  $\hat{P}(\omega)$ . It begins with the generation of a large number of samples of the posterior probability. This is done by starting with a set of uniformly distributed moment tensors and applying the rejection method [von Neumann, 1951; Tarantola, 2005]. The fraction of the resulting moment tensors  $M$  with  $\angle(M_0, M) \leq \omega$  is then  $\hat{P}(\omega)$ . Since  $\hat{P}(\omega)$  can be interpreted in terms of samples of the posterior probability, then so can  $\mathcal{P}(V)$ . For example,  $\mathcal{P}(0.1) = 0.8$  means that 80% of the posterior samples are concentrated in only 10% of the volume around  $M_0$ .

We use samples of the posterior to further characterize and visualize uncertainties associated with our moment tensor solutions. This is best seen in the context of a real example, described next.

## 4. Example Waveform Fits and Uncertainty Analyses

### 4.1. Full Analysis for Example Event

We show the complete results for one of the 21 events in Part I. The event occurred on 7 April 2009 just northwest of Anchorage, Alaska. Results for this event are shown in Figures 5–7. Results for the other 20 Part I events are in *Silwal* [2015].

A subset of waveform fits for our moment tensor inversion are shown in Figure 5; the full set of waveform fits are in *Silwal* [2015]. The observed waveforms are plotted in black, and the synthetic waveforms are red.

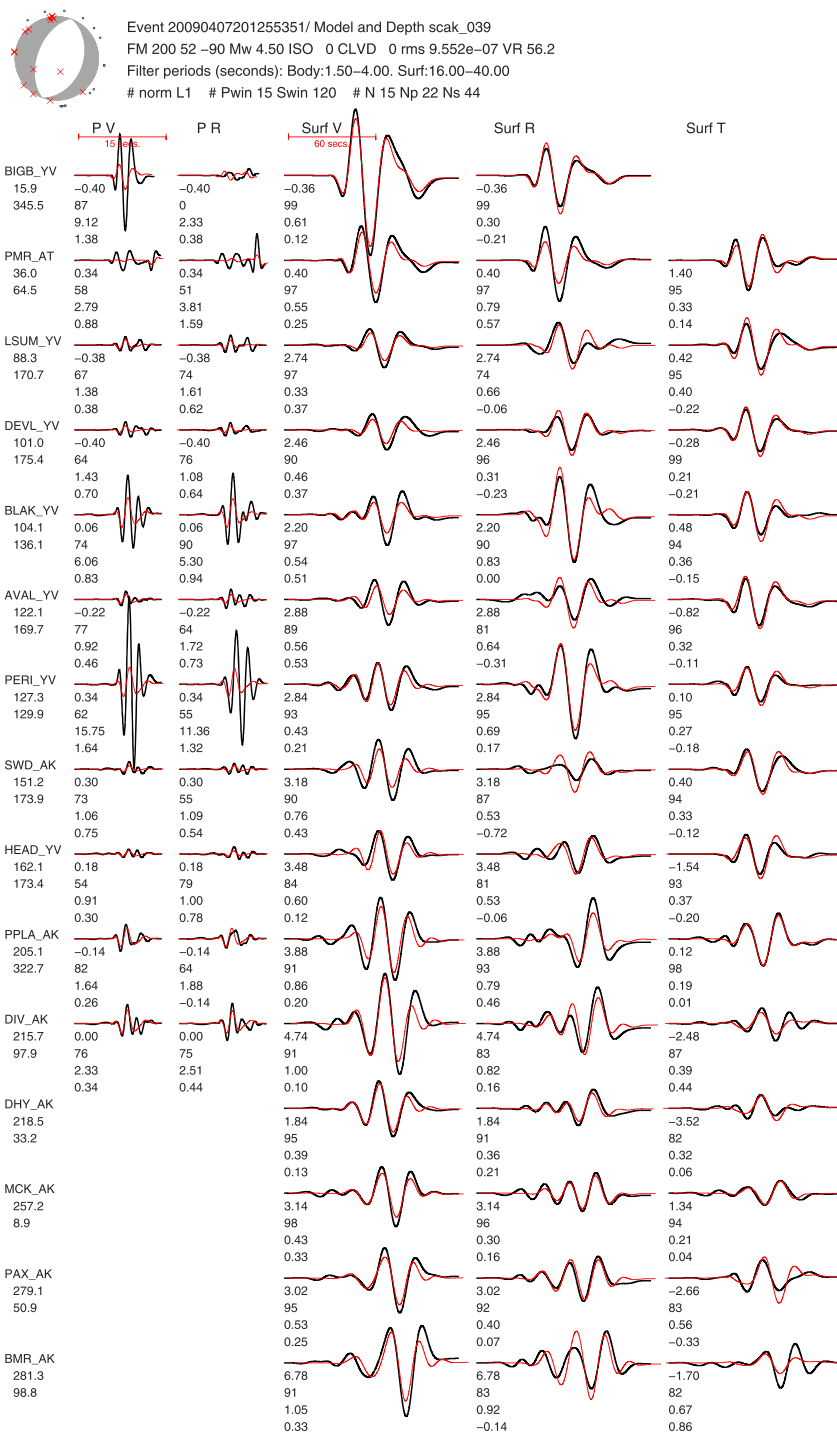


**Figure 5.** Moment tensor solution and waveform comparisons for the example event in this study. Each column is a different section of the three-component waveform: PV = vertical component P wave, PR = radial component P wave, SurfV = vertical component Rayleigh wave, SurfR = radial component Rayleigh wave, and SurfT = transverse component Love wave. The stations are ordered by increasing epicentral distance from the top row. The observed waveforms are plotted in black; the synthetic waveforms are plotted in red. The body waves are filtered 1.5–4.0 s, and the surface waves are filtered 16–40 s. The numbers below each station name are the station epicentral distance (top) and station azimuth (bottom). The four numbers below each pair of waveforms are, from top to bottom, (1) the cross-correlation time shift  $\Delta T = T_{\text{obs}} - T_{\text{syn}}$  required for matching the synthetics  $s(t)$  with the data  $u(t)$  (a positive time shift means that the synthetics arrive earlier than the data); (2) the maximum cross-correlation percentage between  $u(t)$  and  $s(t - \Delta T)$ ; (3) the percentage of the total misfit; and (4) the amplitude ratio  $\ln(A_{\text{obs}}/A_{\text{syn}})$  in each time window. The four header lines are described in Silwal [2015].

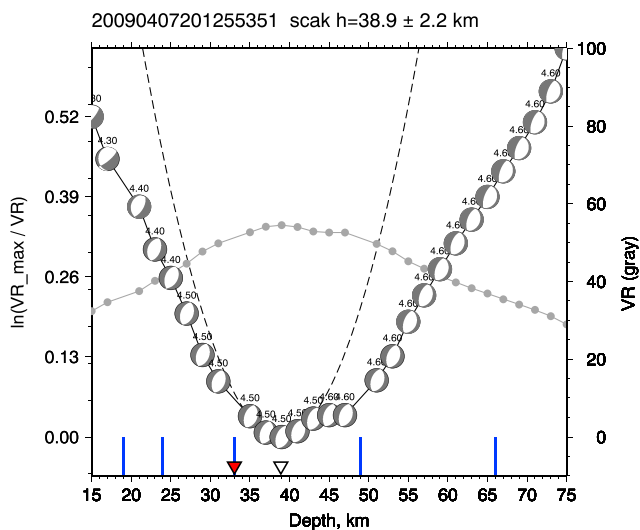


**Figure 6.** Grid search for the best fitting depth for the event in Figure 5. The red inverted triangle marks the AEC catalog depth, and the white inverted triangle marks the depth obtained from our moment tensor inversion. The gray line with solid circles denotes the variance reduction (VR) for the moment tensor solution obtained at that particular depth (scale at right). The best solution occurs at the maximum in variance reduction  $VR_{\max} = 56.2$ . The beach balls are plotted at the value of  $\ln(VR_{\max}/VR)$ , which gives the variance reduction relative to the maximum (scale at left). Note that the orientation and magnitude are free to change for each depth; for this event we see that deeper depths produce larger magnitude estimates (4.6 versus 4.4), as we would expect. The black dashed line is the best fitting parabola, which is used for estimating the uncertainty in depth; here the best fitting depth is  $39 \pm 2$  km. The long tick marks on the x axis mark the layer boundaries in the 1-D model (Table S1) used in the moment tensor inversions.

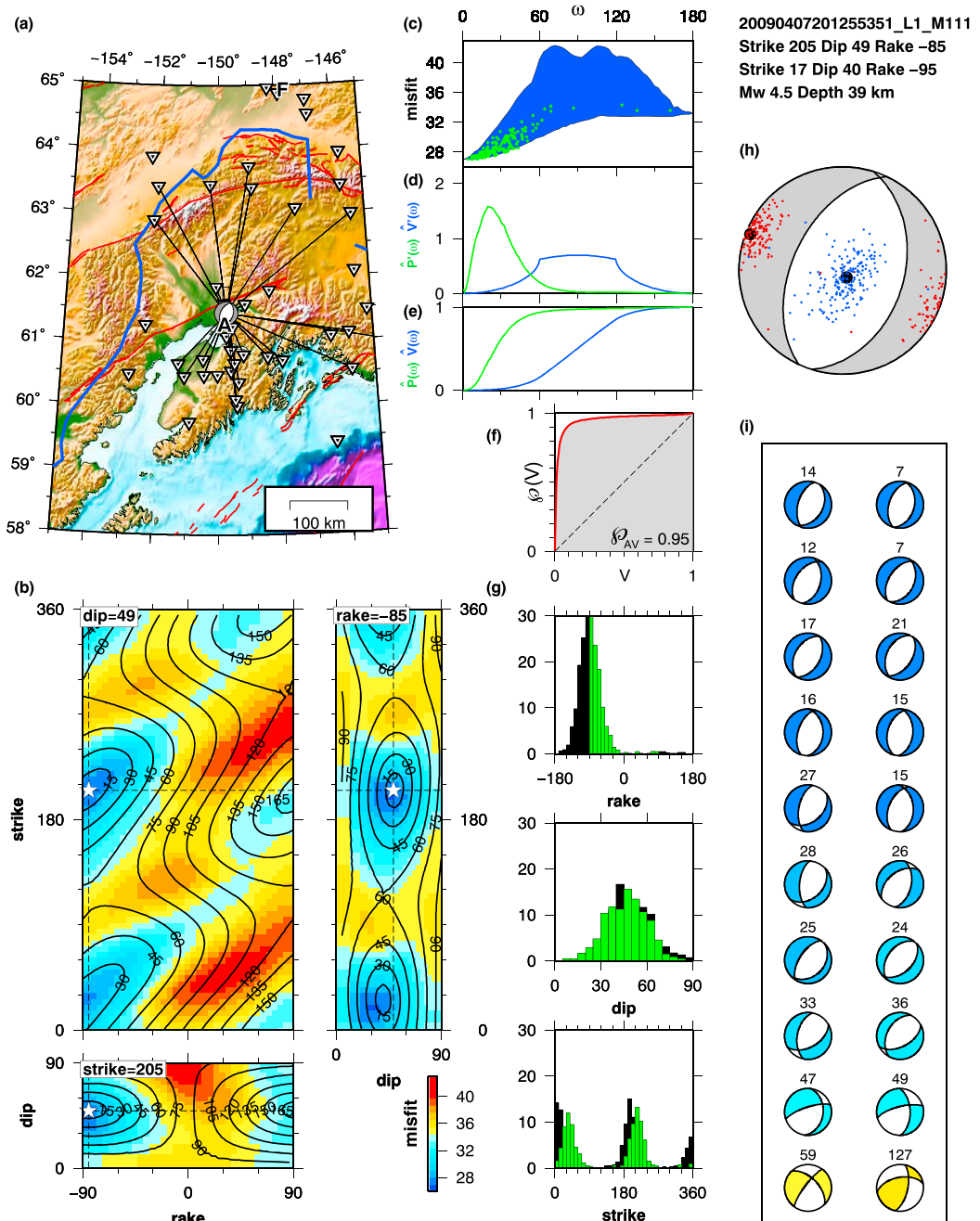
In this example the body waves are filtered 1.5–4.0 s and the surface waves are filtered 16–40 s. The synthetic seismograms have been time shifted by the time shift listed beneath each seismogram pair (section 2.2).

For this event the value of the scaled misfit function (equation (6)) at the global minimum is  $\Phi(M_0) = 27.00$  and the probability density (equation (10)) is  $p(M_0) = 3.30$ . (A related measure, variance reduction, is discussed in section S2.3.) The waveform fits in Figure 5 are good but not exceptional: the probability  $p(M_0) = 3.30$  is exactly in the middle of the 21 events listed in Table 4.

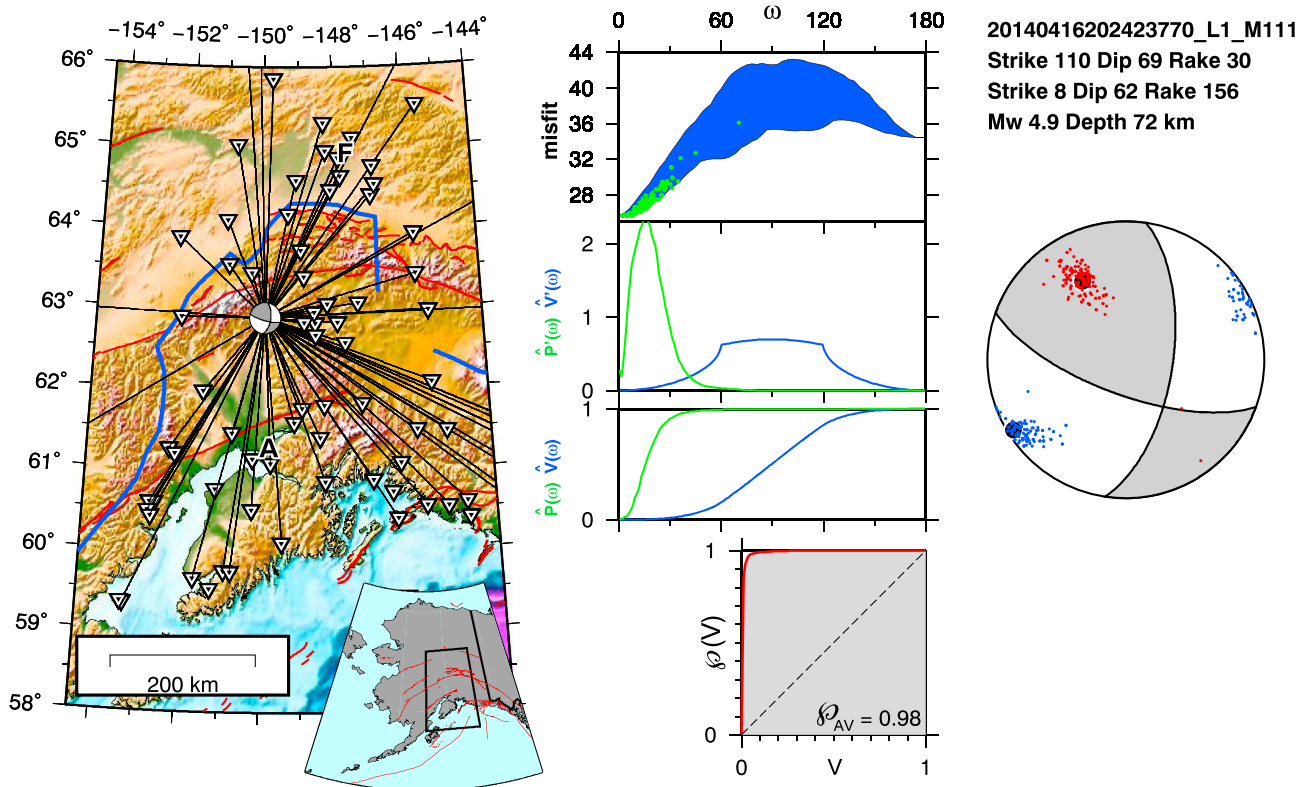
Figure 6 shows the grid search over depth for this event. The depth increment in the grid search is 2 km. For each depth we search over the full space of orientations and magnitudes to obtain the best fitting moment tensor. For this event, the best fitting moment tensor has magnitude  $M_w$  4.5 and occurs at depth 39 km; for comparison, the AEC catalog depth is 33 km, and the AEC moment tensor catalog depth is 45 km.

Figure 7 is a summary of the uncertainty analysis for the event. This analysis is performed after we have determined the best fitting depth and magnitude for the event, and after we have evaluated the misfit function throughout the space of moment tensor orientations. Three cross sections of the strike-rake-dip “brick” are shown in Figure 7b, with colors giving values of the misfit function  $\Phi$ . Each section contains the solution  $M_0$  (white star), which is at  $205^\circ$ , dip  $49^\circ$ ,  $-85^\circ$ . Also shown are contours of the angular distance  $\omega$  from  $M_0$  (equation (9)). They do not correspond to distances in the brick and may at first look peculiar. For example, in the strike-rake cross section the two seemingly separate dark blue patches are close to each other when considered in moment tensor space, as shown by their small values of  $\omega$ . In moment tensor space, the two patches are parts of a single small neighborhood of  $M_0$ . The three light blue patches near the right edge of the strike-rake section are parts of a single small neighborhood of  $-M_0$  when considered in moment tensor space. Incidentally, there are never any repeated moment tensors strictly inside the strike-rake-dip brick; repetitions can only occur on the boundary [Tape and Tape, 2012].

Our uncertainty analysis contains two parts. In the first part (Figures 7e and 7f and part B of Figure 3) we calculate the confidence curve  $\mathcal{P}(V)$  and, from it, the confidence parameter  $\mathcal{P}_{AV}$ : The fractional volume curve  $\hat{V}(\omega)$  and the probability curve  $\hat{P}(\omega)$  (blue and green, respectively, in Figure 7e) are calculated from equations (14) and (15). Then  $\mathcal{P}(V)$  (Figure 7f) is calculated from  $\hat{V}(\omega)$  and  $\hat{P}(\omega)$  using equation (12). The area under the confidence curve gives the average value of  $\mathcal{P}(V)$  (equation (13)), which in this example is  $\mathcal{P}_{AV} = 0.95$ .



**Figure 7.** Summary of the moment tensor solution  $M_0$  for an earthquake near Anchorage. The moment tensor  $M_0$  is the moment tensor with minimum misfit. The set of moment tensors under consideration is the set of double couples. (a) Map showing the earthquake source and the station coverage. The stations used in calculating the misfit are identified with ray paths. (b) Colored map of misfit  $\Phi(M)$ , shown on sections of strike-rake-dip space that pass through the strike-rake-dip point for  $M_0$  (white star). The black curves are not contours of misfit  $\Phi$  but rather contours of  $\omega$ , where  $\omega(M) = \angle(M_0, M)$  is the angular distance from  $M_0$  to  $M$ . (c) A two-dimensional summary of the three-dimensional plot of misfit in Figure 7b. The blue region consists of all pairs  $(\omega(M), \Phi(M))$ . The green dots are pairs  $(\omega(M), \Phi(M))$  for 200 posterior samples. (d) The curves  $\hat{P}(\omega)$  and  $\hat{V}(\omega)$ . (e) The curves  $\hat{V}(\omega)$  and  $\hat{P}(\omega)$ ; they are used to construct the confidence curve  $\mathcal{P}(V)$  in Figure 7f, as explained in Figure 4. (f) The confidence curve  $\mathcal{P}(V)$  for  $M_0$ . The more the curve resembles the shape of a capital gamma ( $\Gamma$ ), the better. The shaded area is the average confidence  $\mathcal{P}_{AV}$ . (g) Strike, rake, and dip for a set of 2000 posterior samples. There are two possible fault normal and slip vector pairs for a double couple; green indicates the pair having its coordinates in the strike-rake-dip box in Figure 7b, and black indicates its conjugate. (h) Beach ball for  $M_0$ . The two big black dots are the  $P$ - $T$  axes of  $M_0$ , and the small red and blue dots are the  $P$ - $T$  axes of 200 posterior samples. (i) The 20 posterior samples. The number above each beach ball  $M$  is its angular distance  $\omega(M)$  from  $M_0$ , and the color of the ball gives its relative misfit, using the same color scale as in Figure 7b.



**Figure 8.** Uncertainty analysis for an event with good station coverage. The figure is like the upper diagram in Figure 7, but for an earthquake near Denali, Alaska. The  $\mathcal{P}(V)$  curve resembles a  $\Gamma$  and gives high confidence ( $\mathcal{P}_{AV} = 0.98$ ) for  $M_0$ . See section 4.2 for details.

The second part of our uncertainty analysis uses samples of the posterior probability, which we generate using the rejection method. Two hundred posterior samples are plotted in the misfit-versus- $\omega$  plot in Figure 7c as green dots; they can be compared with the blue background, which is the corresponding plot for “prior” samples, that is, for uniformly distributed moment tensors. The curves  $\hat{P}(\omega)$  and  $\hat{P}'(\omega)$  (green in Figures 7d and 7e) can both be interpreted in terms of posterior samples: For a large set of posterior samples,  $\hat{P}(\omega)$  is the fraction of them within angular distance  $\omega$  of  $M_0$ , and  $\hat{P}'(\omega) d\omega$  is the fraction of them whose angular distance from  $M_0$  is between  $\omega$  and  $\omega + d\omega$ . A normalized histogram of values  $\angle(M_0, M)$  for posterior samples  $M$  would therefore have the curve  $\hat{P}'(\omega)$  as its upper boundary. In each of Figures 7c–7e, the green color pertains to the posterior probability, and blue pertains to the prior probability, that is, to fractional volume.

A set of 2000 posterior samples is used to plot distributions of strike, dip, and rake in Figure 7g. There are two distributions (green and black), since there are two sets of strike-rake-dip angles for each moment tensor. The global minimum  $M_0$  is plotted as a beach ball in Figure 7h along with  $P$ - $T$  axes for 200 posterior samples. Beach balls for 20 posterior samples are shown in Figure 7i. Stähler and Sigloch [2014] offered a similar perspective by averaging posterior beach balls to get a “Bayesian beach ball.”

#### 4.2. Additional Earthquake Examples

In Figures 8 and 9 we show condensed versions of the uncertainty analysis for two events that are outside our region of interest and not in our catalog. These examples suggest the range in quality of solutions that we might expect in Alaska, and they provide some reference for the values of  $\mathcal{P}_{AV}$ . The first event, a slab earthquake beneath the Alaska Range, represents one of the best possible data sets for a moment tensor inversion in Alaska. For this 2014 earthquake there is complete azimuthal coverage, with 76 stations used in the inversion. The  $\mathcal{P}(V)$  curve resembles  $\Gamma$ , and  $\mathcal{P}_{AV} = 0.98$  is nearly unity (good).

The second event, a crustal earthquake in northwestern Alaska (near Noatak), has poor data coverage, with almost all stations situated within a  $60^\circ$  azimuth of the source. For this event the curve  $\mathcal{P}(V)$  is near the  $45^\circ$  line (Figure 9f), indicating that  $M_0$  is not a reliable solution. This earthquake was well-recorded globally, and the GCMT solution indicated a normal-fault mechanism with  $M_w 5.7$ , whereas the (unreliable) solution in Figure 9

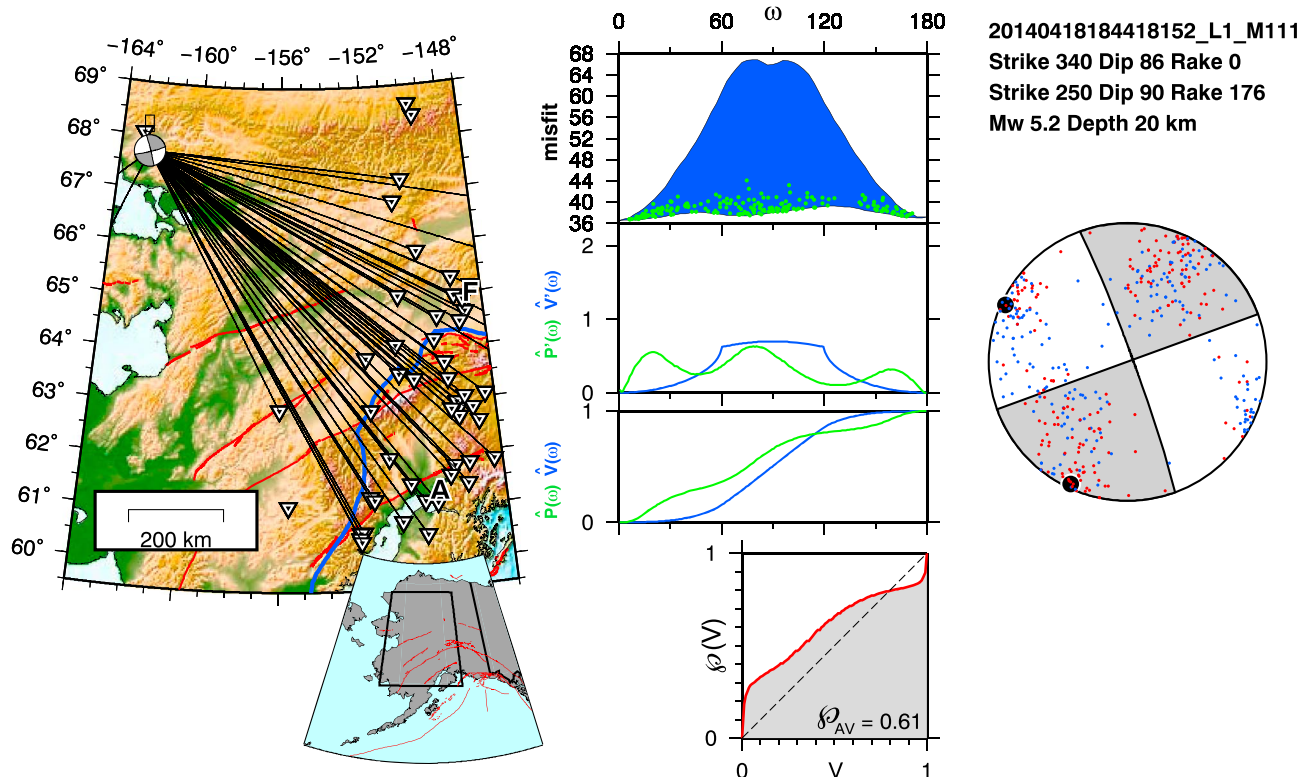


**Figure 9.** Uncertainty analysis for an event with poor station coverage. The figure is like the upper diagram in Figure 7, but for an earthquake near Noatak, Alaska. Examining the curve  $\hat{P}'(\omega)$ , we see that the probability is widely distributed over moment tensor space, which leads to a low confidence ( $\mathcal{P}_{AV} = 0.61$ ) for  $M_0$ . The closeness of  $\hat{P}(V)$  to the 45° line (dashed) is another indication that  $M_0$  is not a reliable solution. See section 4.2 for details.

is a strike-slip mechanism with  $M_w$  5.2. Smaller events, which, like the Noatak earthquake, are near the margins of the Alaska regional network, will not appear in global moment tensor catalogs. In such cases we will need to rely on assessing the confidence of our regional moment tensor solutions.

In Figures 10 and 11 we compare the moment tensor solution and waveform fits from our catalog with those from the AEC moment tensor catalog. The moment tensor in Figure 10 clearly provides better waveform fits, and it results in a larger variance reduction (39% versus 25%). Among the 21 Part I events, the event in Figure 10 had the largest difference ( $\omega = 54^\circ$ ) from the solution in the AEC moment tensor catalog. A visual inspection of the beach balls in Figures 10 and 11 shows that these solutions are quite different and would imply two different tectonic interpretations for this  $M_w$  5.0 earthquake.

## 5. Moment Tensor Catalog: Part I (21 Events)

There are 21 events in the AEC moment tensor catalog that occurred within our region during the time period of interest. For each of these events we perform a range of inversions with different subsets of data, in order to quantify the influence of various factors on the estimated model parameters and their uncertainties. The different types of inversions and comparisons are listed in Tables 1 and 2. We note that the 21 events are all high-quality events:  $M_w \geq 4$  recorded by dozens of stations at regional distances. The inferences we make in the comparisons below may not generalize to the smaller Part II events.

Implicit in these comparisons is our choice of the “best” moment tensor, which we take to be the one whose synthetic seismograms fit the most observed seismograms (this is explained in section 7.3). This corresponds to the  $M_{111}$  case in Table 1. We can then measure the angular difference between another moment tensor to  $M_{111}$ .

We use Table 3 to explain the different inversions for the example event. The different subsets of data produce similar moment tensors, as indicated by  $\omega \leq 26^\circ$  from  $M_{111}$ . However, two cases ( $M_{110}$  and  $M_{101}$ ) have low values of  $p(M_0)$  and  $\mathcal{P}_{AV}$ , and we would not consider these to be reliable solutions. The table also shows the

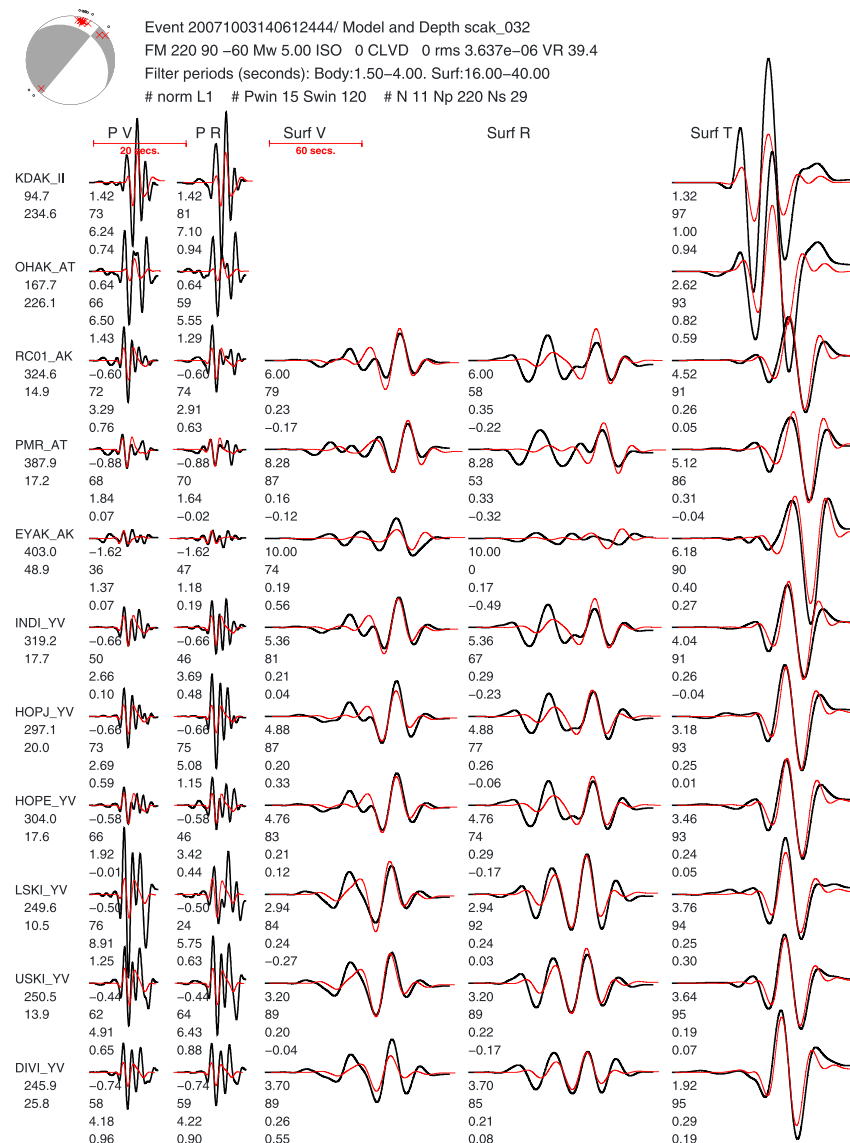


**Figure 10.** Moment tensor solution and waveform fits at a subset of 11 stations for event 20071003140612444 (depth 32 km,  $M_w$  5.0). The angle between this solution and the AEC moment tensor catalog solution is 56°. See Figure A in Silwal [2015] for the waveform fits for the full set of 45 stations. See Figure 11 for the waveform fits when using the AEC moment tensor. See Figure 7 caption for details.

distance of the two AEC catalog moment tensors,  $M_{\text{AEC}}$  and  $M_{\text{fm}}$ , from  $M_{111}$ . Table 3 is reproduced for the other Part I catalog events in Table S3. The information in Table S3 is presented in abridged form in Table 5. We will refer to these results while discussing the six comparisons listed in Table 2.

## 5.1. The Effect of Using Bad Stations

Manual review and selection of waveforms can be an extremely time-consuming part of seismological studies. We expect there to be differences between data and synthetics. Some differences are due to errors in representing the earthquake source or Earth structure, while other differences are due to inherent errors in the observed waveforms for a particular earthquake and a particular station at a particular time. We generally do not know what the estimated errors are in the observed waveforms, but we have some idea of errors in our synthetic seismograms due to errors in our assumed Earth model. For example, in our region the presence of Cook Inlet basin produces larger amplitudes and larger time shifts for source-station paths that interact with the basin. Therefore, some systematic amplitude anomalies may be expected.

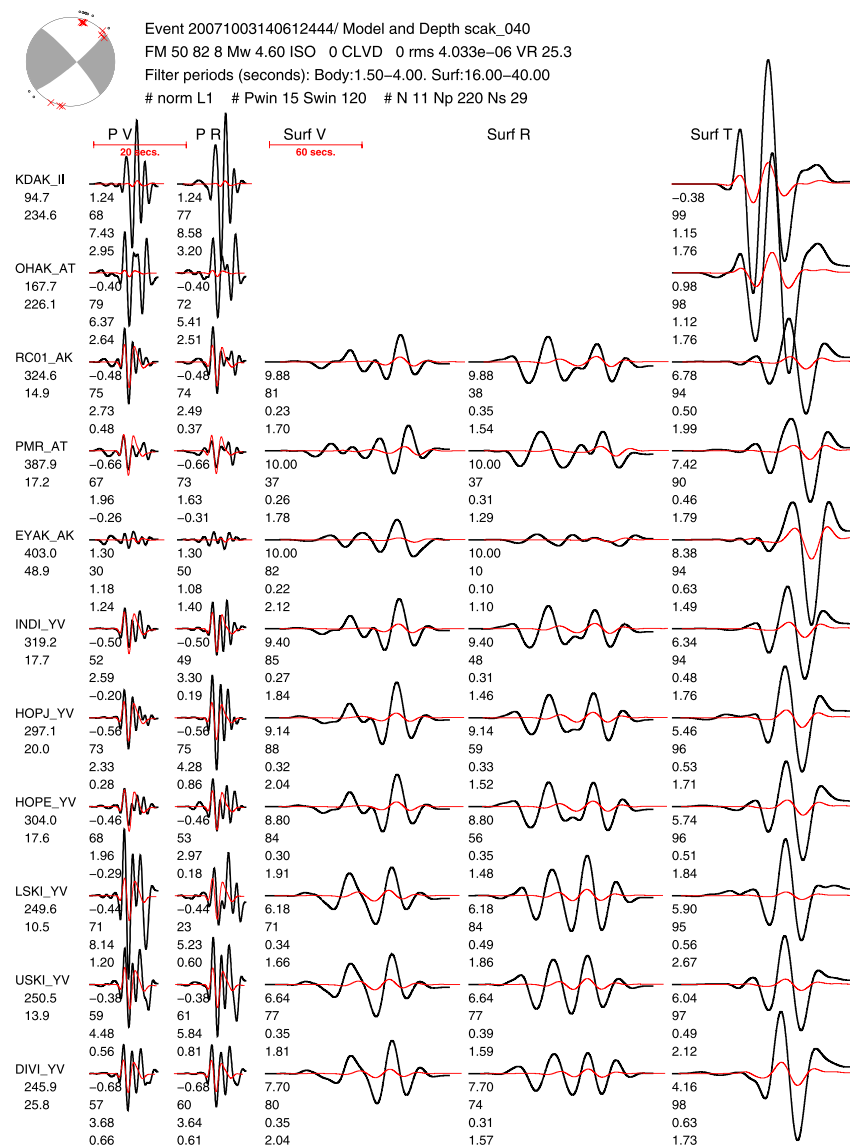


**Figure 11.** Same as Figure 10 but showing synthetic waveforms for the moment tensor and depth (40 km) in the AEC moment tensor catalog. Our preferred moment tensor solution in Figure 10, obtained using both body and surface waves, provides better waveform fits (CAP VR = 39%; AEC VR = 25%). Here we allow the magnitude of the AEC moment tensor to vary in order to achieve the best possible waveform fits for this fixed hypocenter and orientation; the best fitting magnitude of  $M_w$ 4.6 is much lower than  $M_w$ 5.0 in Figure 10. See Figure S4 for the AEC waveform fits when the magnitude is fixed to be the AEC magnitude.

Our motivation for using the L1 misfit function (equation (6)), rather than the L2 misfit function, was to reduce the effort of manually reviewing waveform comparisons [Maceira *et al.*, 2000; Aster *et al.*, 2012; Tarantola, 2005]. In Figure 12 we show inversion results for 21 events for four cases: L1 with good waveforms, L1 with all waveforms, L2 with good waveforms, and L2 with all waveforms. We find that (1) the L2 norm fails dramatically for some events (red beach balls) and (2) the L1 norm gives stable results even when bad stations are not thrown out. Except for Figure 12, all the results presented in this study (Tables 4 and S5) are based on using the L1 norm in the misfit function (equation (6)).

### 5.2. The Effect of Ignoring Body Waves

The effect of ignoring body waves can be seen by comparing the columns of  $M_{111}$  with those of  $M_{011}$  in Table 5. The angular differences range from 0° (three events) to ≥50° (two events). The two anomalous events here are both  $M_w \geq 5.0$ ; one is a slab event to the west with decent station coverage, the other is a crustal

**Table 1.** Moment Tensor Labels Used in the Study to Distinguish Among Inversions Using Different Subsets of Waveform Data<sup>a</sup>

Label	Description
$M_{111}$	using both body and surface waves at selected stations
$M_{011}$	using only surface waves at selected stations
$M_{101}$	using only body waves at selected stations
$M_{112}$	using both body and surface waves at stations used in AEC moment tensor catalog
$M_{012}$	using only surface waves at stations used in AEC moment tensor catalog
$M_{110}$	using both body and surface waves at all stations
$M_{AEC}$	AEC moment tensor catalog (should be close to $M_{012}$ )
$M_{fm}$	AEC first-motion catalog

<sup>a</sup>The three indices in the label  $M_{abc}$  represent the choice of body waves ( $a = 0, 1$ ), the choice of surface waves ( $b = 0, 1$ ), and the choice of stations ( $c = 0, 1, 2$ ). The index  $c$  covers three cases:  $c = 0$  is for all available stations,  $c = 1$  is a subset of stations that pass our waveform selection criteria, and  $c = 2$  is a smaller subset of stations used for the inversions in the AEC moment tensor catalog. See section 5 for details.

event to the southwest with relatively poor station coverage. A further analysis could provide insights into the scenarios where using body waves is particularly important for obtaining the correct moment tensor solution.

### 5.3. The Effect of Using Fewer Stations

The effect of using fewer stations, while using both body waves and surface waves, can be seen by comparing case  $M_{111}$  with  $M_{112}$ . The comparison shows that there are significant differences (five events with  $\omega \geq 50^\circ$ ) in the moment tensor solution when we use fewer stations. In practice, it is not easy to determine which station will “pull” the solution toward the true solution. Our tabulation implies that using as many stations as possible is desirable. It is important to have good azimuthal coverage of stations, but we did not systematically investigate this.

### 5.4. Improvement Over Existing Catalogs

We can also compare the angular difference from our preferred solution ( $M_{111}$ ) to the moment tensors in the two AEC catalogs ( $M_{AEC}$  and  $M_{fm}$ ) (Table 5). For the 21 Part I events the differences with the AEC moment tensor catalog are generally small ( $\omega < 30^\circ$ ), with one exception (20071003140612444:  $\omega = 54^\circ$ ) highlighted in Figures 10 and 11. We discuss catalog comparisons in section 7.4.

### 5.5. The Effect of Using Either Body Waves or Surface Waves

From Figure 13 we see that moment tensor solutions obtained using only surface waves ( $M_{011}$ ) are consistently better than solutions obtained using only body waves ( $M_{101}$ ). Furthermore, the confidence measure  $P_{AV}$  is higher for the surface-wave-only solutions (Table S3).

### 5.6. Additional Comparisons

When considering only surface waves, there is a small effect of adding more stations. This can be seen in Figure 13 for the columns  $M_{012}$  (few stations) and  $M_{011}$  (more stations). This possibly justifies the practice

**Table 2.** Examples of Comparisons Between Different Sets of Moment Tensors Listed in Table 3<sup>a</sup>

Misfit Function		Analysis	
$M_{111}$	versus	$M_{110}$	effect of using bad stations (for testing multiple norms)
$M_{111}$	versus	$M_{011}$	effect of ignoring body waves
$M_{111}$	versus	$M_{112}$	effect of using fewer stations (both body and surface waves)
$M_{111}$	versus	$M_{AEC}$	improvement over existing catalog
$M_{101}$	versus	$M_{011}$	effect of using either body waves or surface waves
$M_{012}$	versus	$M_{011}$	effect of adding more stations (only surface waves)
$M_{012}$	versus	$M_{AEC}$	effect of using a different inversion method with the same seismograms
$M_{AEC}$	versus	$M_{fm}$	comparison between two catalogs (AEC moment tensor and AEC first motion)

<sup>a</sup>See section 5 for details.

**Table 3.** Summary of Inversions for the Example Event (20090407201255351) for the L1 Misfit Function Using Different Subsets of Data<sup>a</sup>

Misfit Function (See Table 1)		Depth (km)	$M_w$	$\omega$ (deg)	$p(M_0)$	$\mathcal{P}_{AV}$
L1	$M_{111}$	39	4.5	–	3.30	0.95
L1	$M_{110}$	39	4.4	26	0.04	0.52
L1	$M_{011}$	41	4.5	9	9.26	0.98
L1	$M_{101}$	39	4.6	21	2.26	0.77
L1	$M_{112}$	39	4.5	10	2.27	0.95
L1	$M_{012}$	47	4.6	10	10.44	0.98
L1	$M_{AEC}$	45	4.6	17	–	–
L1	$M_{fm}$	33	4.5	32	–	–

<sup>a</sup> $\omega = \angle(M_{111}, M)$ , where  $M$  is a different moment tensor solution. Previously published catalog results are included as  $M_{AEC}$  and  $M_{fm}$ ; for these events, no  $p(M_0)$  and  $\mathcal{P}_{AV}$  are listed, since we did not perform the inversion. Table S3 contains similar results for the other Part I events in the catalog. See Figure 7 ( $M_{111}$ ) and Figures S11–S15 ( $M_{110}$ ,  $M_{011}$ ,  $M_{101}$ ,  $M_{112}$ , and  $M_{012}$ ) for the uncertainty analysis for each case  $M_{abc}$ .

of using small (<10) subset stations for surface-wave-only moment tensor inversion [e.g., Dreger *et al.*, 2000; Ratchkovski and Hansen, 2002; Clinton *et al.*, 2006].

For completeness we also compare the effect of using a different inversion code with same seismograms. This is achieved by performing a CAP inversion ( $M_{012}$ ) using the same stations and same band-pass filter as those used in the AEC moment tensor catalog ( $M_{AEC}$ ). Any differences would arise from the minor differences (e.g., how time windows are cut and how stations are weighted by distance) between the CAP algorithm that we use and the TDMT algorithm that is used by AEC. The differences shown in the  $M_{012}$  and  $M_{AEC}$  columns in Figure 13 are small, as we would hope. Note that much of the visual difference arises from comparing a double couple moment tensor ( $M_{012}$ ) to a deviatoric but non–double couple moment tensor.

## 6. Moment Tensor Catalog: Part II (85 Events)

Part I of our moment tensor catalog contains 21 events. For each event we performed a grid search over depth, an uncertainty analysis, and a series of comparison inversions (section 5). Table 4 lists the moment tensor parameters, and Silwal [2015] contains figures of waveform fits, depth grid searches, and uncertainty analyses.

We performed moment tensor inversions for an additional 85 events that make up Part II of our catalog. These events were the largest events within the AEC first-motion catalog (but not within the AEC moment tensor catalog) that occurred during the time period of interest (section 2). For these smaller events we decided to use a limited number of first-motion polarity measurements to help guide the inversion by excluding moment tensors that fail to match the polarities. The moment tensor parameters are listed in Table S5, and waveform fits are provided in Silwal [2015]. In principle it should be possible to perform the uncertainty analyses for a misfit function that uses both waveform differences and first-motion polarities. It would be interesting to see the  $\mathcal{P}_{AV}$  curves for earthquakes with worse data than the high-quality events in Part I. The example in Figure 9 suggests that the uncertainty analysis could provide insights into local minima in the misfit function that may occur.

In the supporting information we provide waveform fits for two Part II catalog events (Figures S5–S7 and Figures S8–S10). These examples show the challenges associated with moment tensor inversions for events with lower signal-to-noise ratios (like smaller events): the waveform fits for two very different moment tensors appear to be qualitatively comparably good. An uncertainty analysis would benefit these events, as would a detailed investigation of the inclusion of first-motion polarities along with the waveforms.

## 7. Discussion

### 7.1. The Confidence Curve $\mathcal{P}(V)$

We provide several examples to elucidate the confidence curve  $\mathcal{P}(V)$ . In all of them we are dealing with double couple moment tensors. The normalized eigenvalues are therefore  $\Lambda=(1, 0, -1)/\sqrt{2}$ , and the fractional

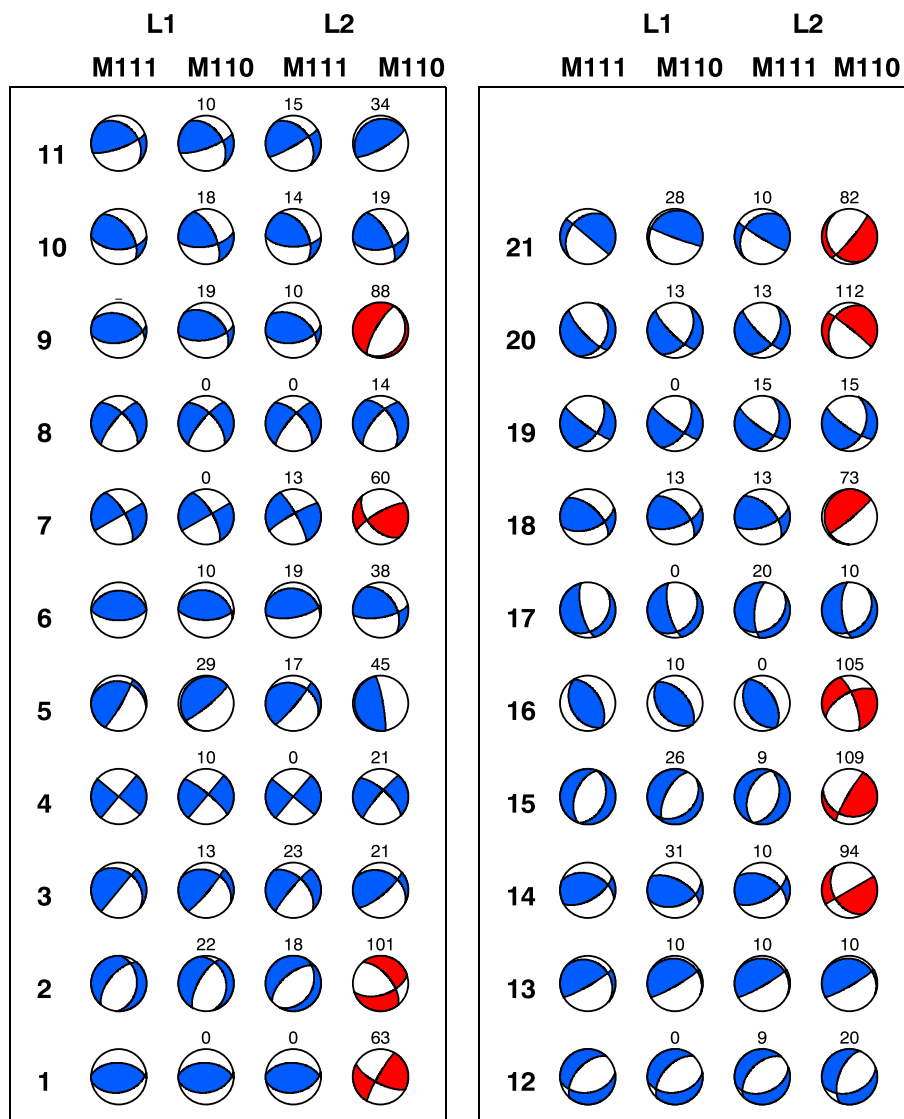


**Figure 12.** The effect of using an L1 versus an L2 norm in the misfit function for the 21 Part I events. (first column) Using only the best stations ( $M_{111}$ ) and applying the L1 norm. (second column) Using all stations ( $M_{110}$ ) and applying the L1 norm. (third column) Using only the best stations ( $M_{111}$ ) and applying the L2 norm. (fourth column) Using all stations ( $M_{110}$ ) and applying the L2 norm. The number above each beach ball is the angle  $\omega$  to the preferred beach ball in Figure 12 (first column); if  $\omega \geq 50^\circ$ , then the ball is colored red and is considered to be significantly wrong.

volume curve  $\hat{V}(\omega)$  takes the shape of a mesa. (The curve will change for full moment tensors or for a different choice of  $\Lambda$  [Tape and Tape, 2016].)

The calculation of  $\mathcal{P}(V)$  is shown in Figure 4. While the curve itself is our indicator of confidence, we also rely on two scalar quantities derived from it. The first is the average  $\mathcal{P}_{AV}$  of  $\mathcal{P}(V)$ ; this is the area under  $\mathcal{P}(V)$ . The second is the slope of  $\mathcal{P}(V)$  at the origin, which is proportional to the probability density at  $M_0$ . Traditionally, an estimated moment tensor  $M$  would be considered good if the curve  $\mathcal{P}(V)$  were steep at the origin. Our philosophy in this paper is that we need to look at the rest of the curve  $\mathcal{P}(V)$  as well; it should be  $\Gamma$ -shaped if  $M$  is truly reliable.

We present three examples of  $\mathcal{P}(V)$  curves in Figures 7–9. Two are for high-quality solutions, where the curves resemble a  $\Gamma$  shape, while one is a low-quality solution, where the curve is close to the  $45^\circ$  line,  $\mathcal{P}(V) = V$ .

Figure 14 shows  $\mathcal{P}_{AV}$  versus  $p(M_0)$  for our 21 events and for all the cases listed in Table 1. The modest correlation seen in the figure suggests that high confidence may reasonably be expected for high  $p(M_0)$ .

**Table 4.** Moment Tensor Catalog, Part I (21 Out of 106 Events), Generated by CAP Using Body Waves and Surface Waves<sup>a</sup>

	Event	Latitude	Longitude	Strike	Dip	Rake	$M_w$	Depth (km)	$p(M_0)$	$\mathcal{P}_{AV}$	$N_s$	
1	20070911234634153	61.53	-151.53	80	40	80	4.4	94	(100.9)	3.19	0.89	37
2	20070919112226549	61.38	-146.11	225	62	-70	4.5	47	(30.8)	2.35	0.92	42
3	20071003140612444	58.28	-151.29	45	83	60	5.0	32	(45.5)	4.38	0.88	45
4	20071010180326301	59.96	-147.41	40	87	5	4.2	27	(11.8)	1.56	0.90	44
5	20071128235703849	61.91	-151.13	35	83	65	4.9	69	(69.6)	7.65	0.97	48
6	20080314093821771	61.07	-152.64	265	28	90	5.1	139	(143.7)	8.28	0.94	38
7	20080327230745201	59.01	-152.17	240	90	-25	5.1	65	(68.5)	1.66	0.90	28
8	20080828231418631	62.12	-149.60	220	76	-30	4.2	54	(43.0)	4.36	0.95	33
9	20080918194353069	59.50	-152.79	75	58	65	4.6	81	(90.2)	0.88	0.78	29
10	20081228071310738	62.35	-151.05	90	54	50	4.6	82	(89.3)	4.28	0.95	21
11	20090124180950811	59.43	-152.89	70	76	55	5.8	105	(97.9)	1.33	0.85	35
12	20090215193500098	61.60	-146.33	80	40	-55	4.5	43	(37.2)	1.80	0.93	59
13	20090223000427175	58.92	-153.63	60	80	75	4.9	81	(87.8)	11.76	0.94	18
14	20090317011333066	60.24	-152.15	60	58	60	4.3	96	(90.1)	0.75	0.78	13
15	20090407201255351	61.45	-149.74	205	50	-85	4.5	39	(33.0)	3.30	0.95	25
16	20090414171427415	60.16	-153.06	145	40	75	4.3	111	(117.8)	0.89	0.83	29
17	20090430045457938	58.99	-151.31	40	28	-45	4.8	40	(52.7)	5.52	0.89	41
18	20090524094004552	59.78	-153.25	70	54	40	4.6	109	(125.5)	2.02	0.89	32
19	20090622192805162	61.94	-150.70	25	50	-20	5.4	62	(64.6)	4.30	0.94	57
20	20090626164820729	61.91	-150.64	25	35	-25	4.2	56	(59.5)	7.72	0.95	27
21	20090730223910267	59.93	-151.09	220	20	15	4.6	60	(44.1)	3.62	0.94	23
Figure 8	20140416202423770	62.89	-149.91	110	69	30	4.9	72	(82.9)	1.77	0.98	76
Figure 9	20140418184418152	63.93	-145.77	340	86	0	5.2	20 <sup>b</sup>	(20)	12.29	0.61	54

<sup>a</sup>The depth is obtained from grid search and is based on variations in the amplitudes of waveforms (e.g., Figure 6). The AEC catalog depth, derived from P and S traveltimes, is listed in parentheses. The last three columns are the maximum probability density ( $p(M_0)$ ), the confidence parameter ( $\mathcal{P}_{AV}$ ), and the number of stations used in the inversion ( $N_s$ ). See Table S5 for the complete catalog of 106 events. Additional inversions with these events are tabulated in Table 5.

<sup>b</sup>For the Noatak event the inversion was performed at the AEC catalog depth.

In geometrical terms, if  $\mathcal{P}(V)$  starts at the origin with a high slope (high  $p(M_0)$ ), then there is a good chance that  $\mathcal{P}(V)$  will result in a  $\Gamma$  shape with its area near 1. Yet it is no guarantee, as illustrated by the Noatak event (Figure 9). But the main message of Figure 14 is that for a given value of the misfit function at the global minimum  $\Phi(M_0)$ —or, more appropriately, the value of the probability density  $p(M_0)$ —we can expect a wide range of values in  $\mathcal{P}_{AV}$ . As we might have hoped in our endeavor,  $\mathcal{P}_{AV}$  provides useful information about the probability density that is not available from just the information at  $M_0$ .

Thus far, we have chosen to calculate  $\mathcal{P}(V)$  for the global minimum of misfit (or highest probability density)  $M_0$ . But we can calculate  $\mathcal{P}(V)$  for any reference tensor  $M$ , and in some cases it may be useful to do so. In the supporting information we show the uncertainty analysis for our example event when choosing the reference moment tensor to be the maximum misfit solution  $M_x$  (Figure S17) and then again when it is the opposite  $-M_0$  of the minimum misfit solution (Figure S18). For  $M_x$  the slope of  $\mathcal{P}(V)$  at the origin is near zero, as expected, yet the average confidence is  $\mathcal{P}_{AV} = 0.66$ , which, although it is not good, it is not as bad as one might expect. One might have hoped that the worst fitting point would also have low confidence (as hinted by Figure 14), but we can understand why this is not the case. If we examine cross sections of the misfit function (Figure S18b), we can see that, as expected, the misfit goes down as we look in any direction away from the moment tensor with maximum misfit. But  $\angle(M_x, M_0) = 74^\circ$ , so  $M_x$  “sees” the region of high probability around  $M_0$  at an angular distance of only about  $74^\circ$ . The curve  $\mathcal{P}(V)$  therefore rises steeply for  $V \approx \hat{V}(74^\circ) = 0.308$ .

The confidence curve for  $-M_0$  is always a 180° rotation of the confidence curve for  $M_0$  [Tape and Tape, 2016]. Since in this example the confidence curve for  $M_0$  resembles a  $\Gamma$  (Figure 7f), then the confidence curve for  $-M_0$  resembles a backward L. And since  $\mathcal{P}_{AV}$  for  $M_0$  was 0.95,  $\mathcal{P}_{AV}$  for  $-M_0$  is only 0.05. The reason for this low

**Table 5.** Angular Difference  $\omega$  Between Our Preferred Solution ( $M_{111}$ ) and Solutions Obtained Using Different Waveform Data Sets<sup>a</sup>

	Event	$\omega = \angle(M_{111}, M)$							
		$M_{111}$	$M_{110}$	$M_{011}$	$M_{101}$	$M_{112}$	$M_{012}$	$M_{AEC}$	$M_{fm}$
1	20070911234634153	–	0	16	0	37	15	21	12
2	20070919112226549	–	22	18	23	20	31	34	21
3	20071003140612444	–	13	62	119	55	61	54	67
4	20071010180326301	–	10	7	53	41	41	19	20
5	20071128235703849	–	29	0	12	16	0	4	77
6	20080314093821771	–	10	50	0	53	43	32	67
7	20080327230745201	–	0	8	68	19	8	11	19
8	20080828231418631	–	0	10	14	19	19	14	13
9	20080918194353069	–	19	11	56	151	10	8	27
10	20081228071310738	–	18	26	17	21	26	25	27
11	20090124180950811	–	10	10	52	20	10	30	29
12	20090215193500098	–	0	12	36	17	17	25	27
13	20090223000427175	–	10	0	110	0	10	26	25
14	20090317011333066	–	31	0	59	55	13	17	19
15	20090407201255351	–	26	9	21	10	10	17	32
16	20090414171427415	–	10	27	125	50	20	24	21
17	20090430045457938	–	0	10	118	28	16	25	65
18	20090524094004552	–	13	24	0	43	24	29	27
19	20090622192805162	–	0	10	24	10	10	13	13
20	20090626164820729	–	13	19	10	14	30	25	20
21	20090730223910267	–	28	10	29	36	30	17	28

<sup>a</sup>The column labels are described in Table 1. See Figure 13 for the corresponding beach balls. See Table S3 for details, including values of  $p(M_0)$  and  $\mathcal{P}_{AV}$ .

value is that as we move away from  $-M_0$  in any direction in moment tensor space, we do not encounter the concentrated probability near  $M_0$  until we are nearly  $180^\circ$  from  $-M_0$ , at which point the  $\mathcal{P}(V)$  curve shoots up toward 1 to make the backward L.

## 7.2. The Misfit Function Scale Factor $k$

The scale factor  $k$  (equation (6)) in the misfit function  $\Phi$  is arbitrary, and it will systematically alter  $\mathcal{P}(V)$ . If  $k$  is near zero, then the probability density will be nearly constant,  $\mathcal{P}(V)$  will be nearly the  $45^\circ$  line, and the moment tensor orientations (depicted in Figures 7h and 7i) will be nearly random. As  $k$  increases,  $\mathcal{P}(V)$  will sharpen toward a  $\Gamma$  shape,  $\mathcal{P}_{AV}$  will correspondingly increase (assuming that  $\mathcal{P}(V)$  was at least slightly favorable to begin with), and the moment tensor orientations will become more consistent. This is a reminder that one can only meaningfully compare  $\mathcal{P}(V)$  (and  $\mathcal{P}_{AV}$ ) for different earthquakes when the misfit function is the same. In our study we fix  $k$  to be the same for all events, and then our results give a relative measure of confidence among all events in the catalog. A similar qualification faces any moment tensor catalog or any study that attempts to compare results from different catalogs (using different misfit functions).

## 7.3. Finding the Best Moment Tensor Solution

We have discussed three factors in determining the quality of a moment tensor solution: (1) the “amount” of the wavefield that is fit within the moment tensor inversion, (2) the confidence curve  $\mathcal{P}(V)$  and its average  $\mathcal{P}_{AV}$ , (3) the difference between observed and synthetic waveforms.

The normalized waveform difference is represented by probability density  $p(M_0)$  and geometrically depicted by the slope  $\mathcal{P}'(0)$  of the confidence curve for  $M_0$ . Our comparison tests in section 5, tabulated in Table S4, show how  $p(M_0)$  tends to decrease as we include more stations, more seismic phases (like body waves), and shorter-period waveforms in the inversion [see also Zahradník and Custódio, 2012]. Yet what we want is to fit

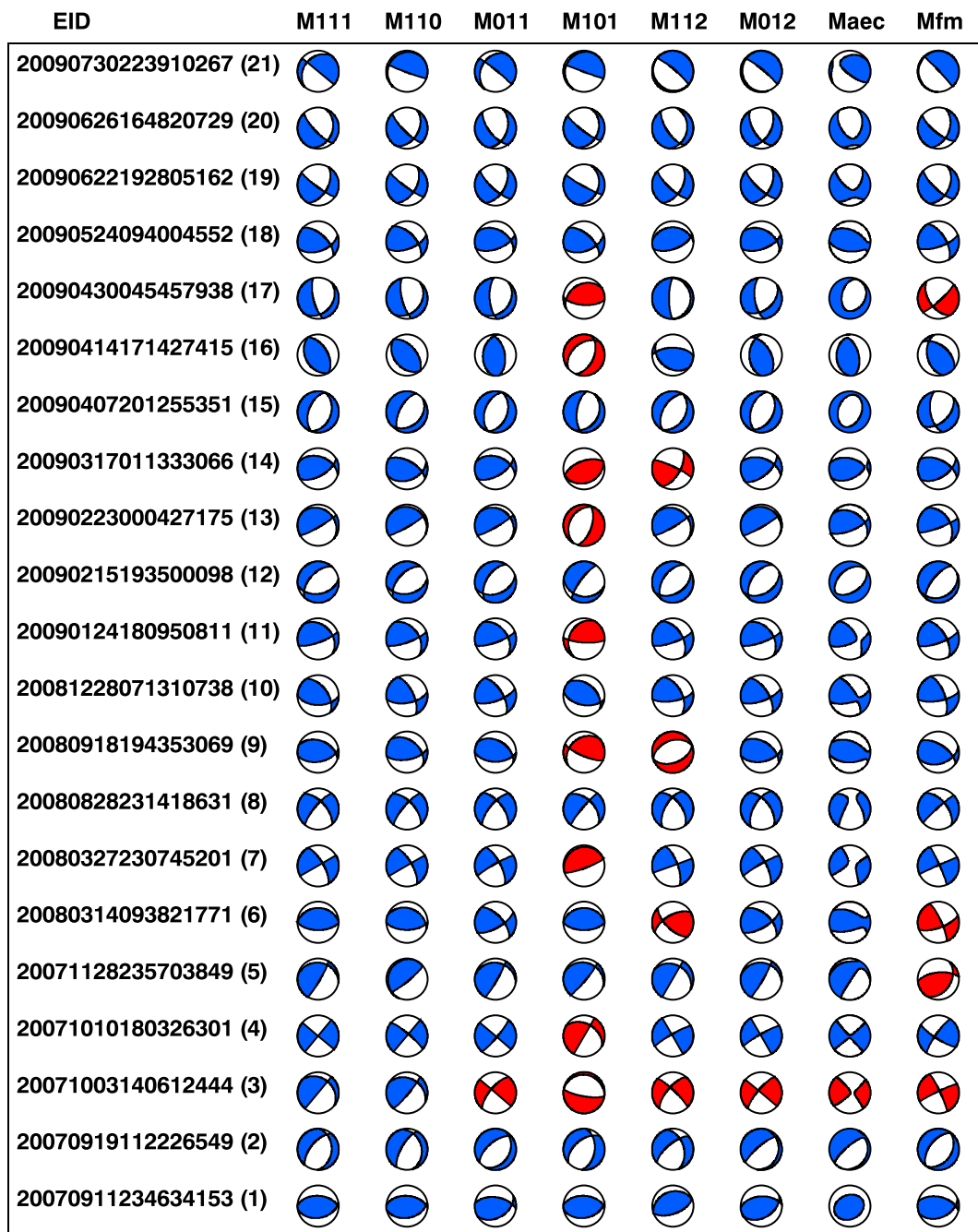


**Figure 13.** Beach balls obtained using different data sets and applying an L1 norm. See Tables 1 and 2 for comparing the differences between different columns. The solution used in our catalog (Table 4) is  $M_{111}$  (the first column). The last two columns show the moment tensors in the Alaska Earthquake Center catalogs ( $M_{AEC}$  and  $M_{fm}$ ). A beach ball is colored red if it is  $\omega \geq 50^\circ$  from the  $M_{111}$  solution.

more of the seismic wavefield, and we cannot simply assume that the moment tensor with the largest  $p(M_0)$  is the better solution. Our guide for establishing our preferred solution  $M_{111}$  is to fit the most waveforms, rather than just to achieve the lowest waveform difference (highest  $p(M_0)$ ). In principle it should be possible to adapt the misfit function to up-weight the amount of time of seismograms used in waveform fitting.

The confidence curve provides insights into the concentration of the posterior probability near  $M_0$ . In the case of the Noatak earthquake (Figure 9), the steep slope of  $\mathcal{P}(V)$  at zero implies a high probability density (low misfit) at  $M_0$ . Yet the confidence curve reveals that  $M_0$  is not a reliable solution.

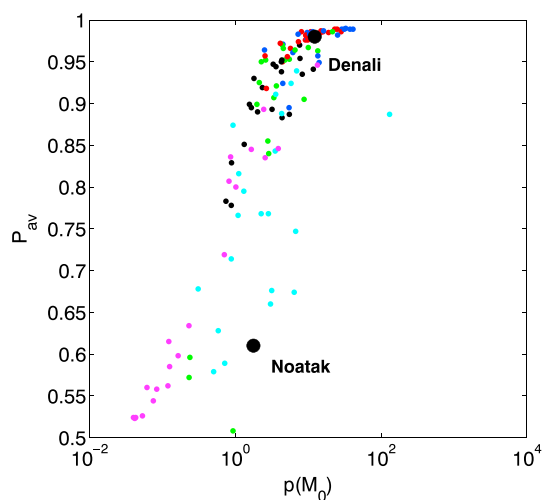


**Figure 14.** Confidence parameter  $P_{AV}$  versus probability density  $p(M_0)$  for the 21 Part I catalog events for inversions performed with different subsets of data (see Table 1):  $M_{111}$  (black),  $M_{011}$  (red),  $M_{101}$  (cyan),  $M_{112}$  (green),  $M_{012}$  (blue), and  $M_{110}$  (magenta). The plot reveals some correlation between  $P_{AV}$  and log-scaled  $p(M_0)$ , though, in general, a range of  $P_{AV}$  values are possible for any given  $p(M_0)$ . See Figure 13 for the set of beach balls corresponding to the dots in this figure. Values for the black dots ( $M_{111}$ ) are listed in Table 4; the two large black dots are for the Denali (Figure 8) and Noatak (Figure 9) events.

magnitudes between our moment tensors and the magnitudes in the AEC catalog (Figure 15d); the average difference 0.2 agrees with Ruppert and Hansen [2010]. Figure S19 shows these different moment tensor catalogs in map view.

We designed this study to provide more than just angular measures between moment tensors in two catalogs. Some of our tests in section 5 allow us to quantify the influence of different choices that are made within a particular approach. To perform one-to-one comparisons, we evaluate the AEC moment tensor ( $M_{AEC}$ ) using the same misfit function as was used to obtain our solution ( $M_{CAP}$ ). By design, the misfit  $\Phi(M_{AEC})$  will always be greater than  $\Phi(M_{CAP})$ , since  $M_{AEC}$  is a point within the global grid search. Our assumption in section 7.3 is that  $M_{CAP}$  is the best solution because it fits the most of the seismic wavefield; therefore,  $M_{AEC}$  will be a worse solution, and we can quantify this difference.

## 8. Summary

We present a catalog of 106 moment tensors in southern Alaska. In order to isolate the impact of decisions made in moment tensor algorithms—stations, band-pass filter, seismic phases, weights, and norm in misfit function—we perform a series of tests in section 5. Our main assumption is that the best solution (section 7.3) is the one that fits the most of the seismic wavefield, in terms of number of stations, number of seismic phases, and broadest range of periods (notably shortest periods). We compare 21 of our moment tensor solutions with those in the Alaska Earthquake Center (AEC) moment tensor catalog, and we compare 85 with the AEC first-motion catalog. We have an inherent advantage over the AEC catalogs in that we use data from the MOOS deployment. We nevertheless can test the influence of choices within the moment tensor inversion by using the same stations as those used in the AEC inversion. Our comparisons are based on the matrix angle between moment tensors; for example,  $\omega = \angle(M_{CAP}, M_{AEC})$  is the angle between our preferred solution derived from the CAP [Zhu and Helmberger, 1996] and the AEC moment tensor solution derived from TDMT [Dreger and Woods, 2002; Ratchkovski and Hansen, 2002].

When comparing two moment tensors, “close enough” depends strongly on how one intends to use the information. If one is interested in understanding the tectonics of a region, then it may be enough to say, for example, that an earthquake is a normal-fault mechanism. In that case  $\omega < 50^\circ$  may be acceptable. If, however,

## 7.4. Comparison of Catalogs

The availability of two different catalogs from the Alaska Earthquake Center allows us to make comparisons with the solutions from our catalog. At the simplest level, we can compare the angular differences among moment tensors for the same event in each catalog. Figure 15a shows a comparison between the AEC moment tensor catalog ( $M_{AEC}$ ) and the AEC first-motion catalog ( $M_{fm}$ ) for the 21 Part I events in our study. These can be seen in Table 5 and in Figure 13 (last two columns), and it is clear that in some cases there are notable differences. Keep in mind that the techniques for estimating these moment tensors are very different: one technique uses long-period ( $T > 16$ s for  $M_w > 4$ ) surface waves, while the other technique uses first-motion  $P$  polarities from raw waveforms.

A direct comparison between our catalog and the AEC moment tensor catalog is shown in Figure 15b for 21 events. A direct comparison between our catalog and the AEC first-motion catalog is shown in Figure 15c for 85 events. We identify a small discrepancy in

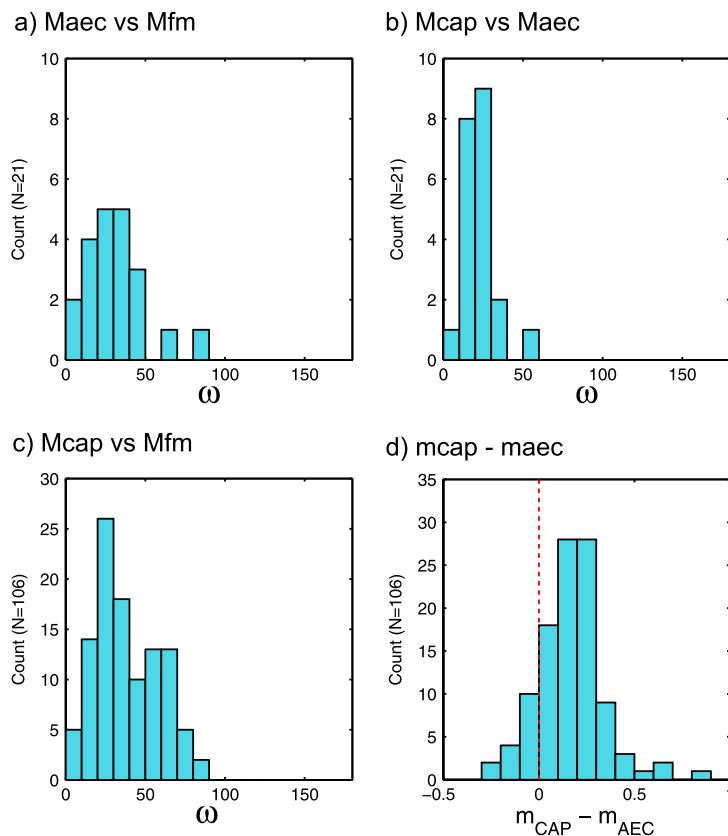


**Figure 15.** Comparison among three moment tensor catalogs for earthquakes in this study: (1) the Alaska Earthquake Center moment tensor catalog ( $M_{AEC}$ ), (2) the AEC first-motion catalog ( $M_{fm}$ ), and (3) our catalog ( $M_{CAP}$ ). The difference between two moment tensors for the same event is quantified by the matrix angle  $\omega$  between the closest double couple moment tensors. (Only the  $M_{AEC}$  moment tensors allow for a non–double couple component.)  
 (a)  $\omega = \angle(M_{CAP}, M_{AEC})$ : AEC first-motion solution versus AEC moment tensor for the 21 Part I events. This shows the influence of using long-period waveforms or first-motion polarities. These results are computed directly from the AEC catalogs. (b) CAP moment tensor versus AEC moment tensor for the 21 Part I events. (c) CAP moment tensor versus AEC first-motion solution for all 106 events. The differences are larger than those in Figure 15b, likely because the set of 106 events includes smaller events than the higher-quality, larger events in Figure 15b. Larger uncertainties in either the CAP solutions or the AEC first-motion solutions will result in larger differences between the two sets of solutions.  
 (d) Differences in magnitude,  $m_{CAP} - m_{AEC}$ , for all 106 events in the catalog. The average difference in magnitude is 0.2, indicating that our CAP magnitude estimates tend to be larger than those from AEC. It is possible that these differences are partly due to how the magnitudes are determined:  $m_{CAP}$  is measured as moment magnitude ( $M_w$ ), and  $m_{AEC}$  is measured as local magnitude ( $M_l$ ).

one is performing a tomographic inversion based on amplitude and traveltime differences, or if one is interested in calculating ground motions from a 3-D wavefield simulation, then it is important to have the best possible moment tensor; this will minimize the propagation of errors from the moment tensor to the seismic velocity structure, or to the ground motion predictions. For these purposes one might want the moment tensor to be  $\omega < 20^\circ$  of the true solution. Our motivation for this study is to use this catalog for a tomographic inversion using wavefield simulations and adjoint methods [e.g., Tape *et al.*, 2009; Lee *et al.*, 2014]. Our improved moment tensor catalog will allow us to more confidently associate differences in traveltimes and amplitudes with structural differences within a 3-D reference Earth model. An additional consideration in such studies is whether to perform additional moment tensor inversions using the 3-D reference model [Liu *et al.*, 2004; Chen *et al.*, 2005; Covellone and Savage, 2012; Zhu and Zhou, 2016].

Three summary points are as follows:

1. We present an improved catalog of moment tensors in southern Alaska. We use both body waves and surface waves from as many broadband stations as possible (both permanent and temporary). Examples in

section 5 show that using more stations and using body waves, in addition to surface waves, can substantially improve the moment tensor solutions. For 33 (out of 106) events, our moment tensor differed from the AEC first-motion solution by  $\omega \geq 50^\circ$  (Figure 15).

2. We demonstrate that using an L1 norm in the misfit function will provide more stable moment tensor solutions (section 2.4 and section 5.1). This should allow for less manual (or automatic) thresholding of bad stations, which could be valuable in operational settings. The modification to the misfit function in the code is trivial.
3. We introduce an approach for quantifying and visualizing the uncertainty in a double couple moment tensor solution (section 3 and Figure 7). The confidence curve  $\mathcal{P}(V)$  in Figure 7f is shaped like a  $\Gamma$  for a high-quality event, and it is close to the 45° line for a low-quality event. The slope of  $\mathcal{P}(V)$  at the origin is related to the probability density at the best fitting moment tensor, and the area under the curve  $\mathcal{P}(V)$  provides the average confidence [Tape and Tape, 2016]. Results for 21 events are presented in Silwal [2015] and summarized in Table 4.

## Acknowledgments

We thank Geoff Abers and Doug Christensen for collecting the seismic waveform data from the MOOS project [Christensen et al., 2008; Li et al., 2013]. Seismic waveforms were obtained from the Alaska Earthquake Center, and they are also available from the IRIS Data Management Center. This project was supported by the Alaska Earthquake Center (V. Silwal) and by a grant from the National Science Foundation (EAR 1251971). We benefitted from discussions with Celso Alvizuri, Natalia Ruppert, Michael West, and Walt Tape. We thank two anonymous reviewers for their constructive feedback.

## References

- Aki, K., and P. G. Richards (1980), *Quantitative Seismology, Theory and Methods*, W. H. Freeman, San Francisco, Calif.
- Aster, R. C., B. Borchers, and C. H. Thurber (2012), *Parameter Estimation and Inverse Problems*, 2nd ed., Elsevier, Waltham, Mass.
- Chen, P., T. H. Jordan, and L. Zhao (2005), Finite-moment tensor of the 3 September 2002 Yorba Linda earthquake, *Bull. Seismol. Soc. Am.*, 95(3), 1170–1180, doi:10.1785/0120040094.
- Christensen, D., G. Abers, and J. Freymueller (2008), Multidisciplinary observations of subduction (MOOS) experiment in south-central Alaska, *Eos Trans. AGU*, 89(53), Fall Meet. Suppl., Abstract U51B-0041.
- Clinton, J. F., E. Hauksson, and K. Solanki (2006), An evaluation of the SCSN moment tensor solutions: Robustness of the  $M_w$  magnitude scale, style of faulting, and automation of the method, *Bull. Seismol. Soc. Am.*, 96(5), 1689–1705, doi:10.1785/0120050241.
- Covellone, B. M., and B. Savage (2012), A quantitative comparison between 1D and 3D source inversion methodologies: Application to the Middle East, *Bull. Seismol. Soc. Am.*, 102(5), 2189–2199, doi:10.1785/0120110278.
- Dreger, D., and B. Woods (2002), Regional distance seismic moment tensors of nuclear explosions, *Tectonophysics*, 356, 139–156, doi:10.1016/S0040-1951(02)00381-5.
- Dreger, D., R. Uhrhammer, M. Pasmanik, J. Franck, and B. Romanowicz (1998), Regional and far-regional earthquake locations and source parameters using sparse broadband networks: A test on the Ridgecrest sequence, *Bull. Seismol. Soc. Am.*, 88(6), 1353–1362.
- Dreger, D. S., H. Tkalcic, and M. Johnson (2000), Dilatational processes accompanying earthquakes in the Long Valley Caldera, *Science*, 288, 122–125.
- Dufumier, H., and L. Rivera (1997), On the resolution of the isotropic component in moment tensor inversion, *Geophys. J. Int.*, 131, 595–606.
- Duputel, Z., L. Rivera, H. Kanamori, and G. Hayes (2012), W phase source inversion for moderate to large earthquakes, *Geophys. J. Int.*, 189, 1125–1147.
- Ekström, G., M. Nettles, and A. M. Dziewoński (2012), The global GCMT project 2004–2010: Centroid-moment tensors for 13,017 earthquakes, *Phys. Earth Planet. Inter.*, 200–201, 1–9, doi:10.1016/j.pepi.2012.04.002.
- Fukuyama, E., and D. S. Dreger (2000), Performance test of an automated moment tensor determination system for the future “Tokai” earthquake, *Earth Planets Space*, 52, 383–392, doi:10.1186/BF03352250.
- Fukuyama, E., M. Ishida, D. S. Dreger, and H. Kawai (1998), Automated seismic moment tensor determination by using on-line broadband seismic waveforms, *J. Seismol. Soc. Jpn.*, 51, 149–156.
- Hardebeck, J. L., and P. M. Shearer (2002), A new method for determining first-motion focal mechanisms, *Bull. Seismol. Soc. Am.*, 92(6), 2264–2276, doi:10.1785/0120010200.
- Haskell, N. (1964), Total energy and energy spectral density of elastic wave radiation from propagating faults, *Bull. Seismol. Soc. Am.*, 54, 1811–1842.
- Helberger, D. V., and G. R. Engen (1980), Modeling the long-period body waves from shallow earthquakes at regional ranges, *Bull. Seismol. Soc. Am.*, 70, 1699–1714.
- Isacks, B., J. Oliver, and L. R. Sykes (1968), Seismology and the new global tectonics, *J. Geophys. Res.*, 73, 5855–5899.
- Kagan, Y. Y. (1991), 3-D rotation of double-couple earthquake sources, *Geophys. J. Int.*, 106, 709–716, doi:10.1111/j.1365-246X.1991.tb06343.x.
- Käufl, P., A. P. Valentine, T. B. O’Toole, and J. Trampert (2014), A framework for fast probabilistic centroid-moment-tensor determination–inversion of regional static displacement measurements, *Geophys. J. Int.*, 196, 1676–1693, doi:10.1093/gji/gjt473.
- Koehler, R. D., R.-E. Farrell, P. A. C. Burns, and R. A. Combellick (2012), Quaternary faults and folds in Alaska: A digital database, *Miscellaneous Publ.* 141, 31 p., Alaska Div. Geol. Geophys. Surv., Fairbanks, Alaska.
- Lee, E.-J., P. Chen, T. H. Jordan, P. B. Maechling, M. A. M. Denolle, and G. C. Beroza (2014), Full-3-D tomography for crustal structure in Southern California based on the scattering-integral and the adjoint-wavefield methods, *J. Geophys. Res. Solid Earth*, 119, 6421–6451, doi:10.1002/2014JB011346.
- Li, J., G. A. Abers, Y. Kim, and D. Christensen (2013), Alaska megathrust 1: Seismicity 43 years after the great 1964 Alaska megathrust earthquake, *J. Geophys. Res. Solid Earth*, 118, 4861–4871, doi:10.1002/jgrb.50358.
- Liu, Q., J. Polet, D. Komatsitsch, and J. Tromp (2004), Spectral-element moment tensor inversions for earthquakes in Southern California, *Bull. Seismol. Soc. Am.*, 94(5), 1748–1761, doi:10.1785/012004038.
- Maceira, M., C. J. Ammon, and R. B. Herrmann (2000), Faulting parameters of the September 25, 1998 Pymatuning, Pennsylvania earthquake, *Seismol. Res. Lett.*, 71(6), 742–752.
- Nayak, A., and D. S. Dreger (2014), Moment tensor inversion of seismic events associated with the sinkhole at Napoleonville salt dome, Louisiana, *Bull. Seismol. Soc. Am.*, 104(4), 1763–1776, doi:10.1785/0120130260.
- Pasyanos, M. E., D. S. Dreger, and B. Romanowicz (1996), Toward real-time estimation of regional moment tensors, *Bull. Seismol. Soc. Am.*, 86(5), 1255–1269.
- Ratchkovski, N. A., and R. A. Hansen (2002), New constraints on tectonics of interior Alaska: Earthquake locations, source mechanisms, and stress regime, *Bull. Seismol. Soc. Am.*, 92(3), 998–1014, doi:10.1785/0120010182.

- Reasenberg, P., and D. Oppenheimer (1985), FPFIT, FPPILOT and FPPAGE: Fortran computer programs for calculating and displaying earthquake fault-plane solutions, *Open File Rep. 85-739*, U.S. Geol. Surv., Denver, Colo.
- Reyes, C. G., and M. E. West (2011), The waveform suite: A robust platform for manipulating waveforms in MATLAB, *Seismol. Res. Lett.*, *82*, 104–110, doi:10.1785/gssrl.82.1.104.
- Riedesel, M. A., and T. H. Jordan (1989), Display and assessment of seismic moment tensors, *Bull. Seismol. Soc. Am.*, *79*(1), 85–100.
- Ristau, J. (2008), Implementation of routine regional moment tensor analysis in New Zealand, *Seismol. Res. Lett.*, *79*(3), 400–415, doi:10.1785/gssrl.79.3.400.
- Ristau, J., G. C. Rogers, and J. F. Cassidy (2007), Stress in western Canada from regional moment tensor analysis, *Can. J. Earth Sci.*, *44*, 127–148, doi:10.1139/E06-057.
- Ross, Z. E., Y. Ben-Zion, and L. Zhu (2015), Isotropic source terms of San Jacinto fault zone earthquakes based on waveform inversions with a generalized CAP method, *Geophys. J. Int.*, *200*, 1267–1278, doi:10.1093/gji/ggu460.
- Rueda, J., and J. Mezcua (2005), Near-real-time seismic moment-tensor determination in Spain, *Seismol. Res. Lett.*, *76*(4), 455–465, doi:10.1785/gssrl.76.4.455.
- Ruppert, N. A., and R. A. Hansen (2010), Temporal and spatial variations of local magnitudes in Alaska and Aleutians and comparison with body-wave and moment magnitudes, *Bull. Seismol. Soc. Am.*, *100*(3), 1174–1183, doi:10.1785/0120090172.
- Scognamiglio, L., E. Tinti, and A. Michelini (2009), Real-time determination of seismic moment tensor for the Italian region, *Bull. Seismol. Soc. Am.*, *99*(4), 2223–2242, doi:10.1785/0120080104.
- Shellenbaum, D. P., L. S. Gregersen, and P. R. Delaney (2010), Top Mesozoic unconformity depth map of the Cook Inlet Basin, Alaska, *Rep. of Invest. RI 2010-2*, Alaska Div. of Geol. and Geophys. Surv., doi:10.14509/21961.
- Silwal, V. (2015), Seismic moment tensor catalog for southern Alaska, ScholarWorksUA. [Available at <http://hdl.handle.net/11122/6025>], last accessed 2016/01/22: descriptor file, text file of catalog, figures with waveform fits, depth searches, and uncertainty analyses.
- Stähler, S. C., and K. Sigloch (2014), Fully probabilistic seismic source inversion—Part 1: Efficient parameterisation, *Solid Earth*, *5*, 1055–1069, doi:10.5194/se-5-1055-2014.
- Tan, Y., L. Zhu, D. V. Helmberger, and C. K. Saikia (2006), Locating and modeling regional earthquakes with two stations, *J. Geophys. Res.*, *111*, B01306, doi:10.1029/2005JB0037750.
- Tape, C., Q. Liu, A. Maggi, and J. Tromp (2009), Adjoint tomography of the Southern California crust, *Science*, *325*, 988–992, doi:10.1126/science.1175298.
- Tape, W., and C. Tape (2012), A geometric setting for moment tensors, *Geophys. J. Int.*, *190*, 476–498, doi:10.1111/j.1365-246X.2012.05491.x.
- Tape, W., and C. Tape (2013), The classical model for moment tensors, *Geophys. J. Int.*, *195*, 1701–1720, doi:10.1093/gji/ggt302.
- Tape, W., and C. Tape (2015), A uniform parameterization of moment tensors, *Geophys. J. Int.*, *202*, 2074–2081, doi:10.1093/gji/ggv262.
- Tape, W., and C. Tape (2016), A confidence parameter for seismic moment tensors, *Geophys. J. Int.*, *205*, 938–953, doi:10.1093/gji/ggw057.
- Tarantola, A. (2005), *Inverse Problem Theory and Methods for Model Parameter Estimation*, SIAM, Philadelphia, Pa.
- Valentine, A. P., and J. Trampert (2012), Assessing the uncertainties on seismic source parameters: Towards realistic error estimates for centroid-moment-tensor determinations, *Phys. Earth Planet. Inter.*, *210*–*211*, 36–49, doi:10.1016/j.pepi.2012.08.003.
- von Neumann, J. (1951), Various techniques used in connection with random digits, in *Monte Carlo Method*, *Appl. Math. Ser.*, vol. 12, edited by A. S. Householder, G. E. Forsythe, and H. H. Germond, U.S. Dept. Commerce Nat. Bur. Stand., Washington, D. C.
- Zahradník, J., and S. Custódio (2012), Moment tensor resolvability: Application to southwest Iberia, *Bull. Seismol. Soc. Am.*, *102*(3), 1235–1254, doi:10.1785/0120110216.
- Zhao, L.-S., and D. V. Helmberger (1994), Source estimation from broadband regional seismograms, *Bull. Seismol. Soc. Am.*, *84*(1), 91–104.
- Zhu, L., and X. Zhou (2016), Seismic moment tensor inversion using 3D velocity model and its application to the 2013 Lushan earthquake sequence, *Phys. Chem. Earth*, doi:10.1016/j.pce.2016.01.002, in press.
- Zhu, L., and D. Helmberger (1996), Advancement in source estimation techniques using broadband regional seismograms, *Bull. Seismol. Soc. Am.*, *86*(5), 1634–1641.
- Zhu, L., and L. A. Rivera (2002), A note on the dynamic and static displacements from a point source in multilayered media, *Geophys. J. Int.*, *148*, 619–627, doi:10.1046/j.1365-246X.2002.01610.x.